





Yb₃Rh₄Sn₁₃: Two-gap superconductor with a complex Fermi surfaceRoman Gumeniuk ^{1,*}, Volodymyr Levvytskyi ¹, Bohdan Kundys ², and Andreas Leithe-Jasper ³¹*Institut für Experimentelle Physik, TU Bergakademie Freiberg, Leipziger Straße 23, 09596 Freiberg, Germany*²*Université de Strasbourg, CNRS, Institut de Physique et Chimie des Matériaux de Strasbourg, UMR 7504, Strasbourg F-67000, France*³*Max-Planck-Institut für Chemische Physik fester Stoffe, Nöthnitzer Straße 40, 01187 Dresden, Germany*

(Received 14 July 2023; revised 10 November 2023; accepted 16 November 2023; published 11 December 2023)

Structural and physical properties of the Yb₃Rh₄Sn₁₃ Remeika phase are investigated on large single crystals grown from Sn-flux. It crystallizes with disordered Y₃Co₄Ge₁₃ structure type [space group *Pm3̄n*, *a* = 9.6709(2) Å], where the 24*k* crystallographic site occupied by Sn atoms is split. Yb₃Rh₄Sn₁₃ is a superconductor (SC) with the critical temperature $T_c = 7.63(5)$ K, lower [$B_{c1} = 14.5(5)$ mT] and upper [$B_{c2}(0) = 2.89(5)$ T] critical fields, as well as a clear peak effect with $B^*(0) = 1.96(9)$ T observed in the $M(H)$ loops. $B_{c2}(T_c)$ can be described by the sum of two Werthamer-Helfand-Hohenberg equations. A $\gamma(B) \propto B^{0.75}$ dependency is found. The electronic specific heat below T_c follows an exponential function including 87% of a strongly coupled [$\Delta_1/k_B T_c = 3.52(1)$] and 13% of a conventional *s*-wave-like [$\Delta_2/k_B T_c = 1.32(1)$] gap. The observations are in line with Yb₃Rh₄Sn₁₃ being a two-gap SC. The Remeika phase reveals a complex electronic band structure studied by Hall coefficient (R_H) measurements and calculations performed within the density functional theory. A “rattling” effect in Yb₃Rh₄Sn₁₃ is discussed based on structural refinements and phononic contributions to its specific heat capacity.

DOI: [10.1103/PhysRevB.108.214515](https://doi.org/10.1103/PhysRevB.108.214515)**I. INTRODUCTION**

In the early 1980s Remeika and co-workers discovered a family of intermetallics crystallizing with the primitive cubic Yb₃Rh₄Sn₁₃ type [1]. Being structurally akin to simple perovskite [2] and filled skutterudite [3] types this stannide is considered as so-called cage compound, where enlarged [Sn₁₂] icosahedra incorporate a “rattling” Sn atoms. This family of intermetallics comprises more than 100 compounds, a few dozen of which are superconductors with the critical temperatures (T_c) up to ~ 10 K and frequently unconventional mechanisms [4], which comes without surprise considering analogous behaviors in cage compounds [5–12].

Superconductivity at $T_c = 8.6$ K with an upper critical field $B_{c2} = 3.5$ T was reported for Yb₃Rh₄Sn₁₃ in a seminal publication of Remeika *et al.* [1]. However, further studies found both these parameters somewhat lower (i.e., $T_c = 7.8$ K, $B_{c2} = 2.6$ T) [13,14] as well as detected a hysteretic peak effect (PE) above a finite reversible field region (i.e., B^*) in the magnetization, which is suppressed with increasing temperature. This finding indicated a clear tricritical point at $T_t \approx 6$ K in the B_{c2} – T_c phase diagram, starting from which B_{c2} and B^* deviate upward and downward, respectively. Such a phase diagram is a hallmark of a Fulde-Ferrel-Larkin-Ovchinnikov (FFLO) superconducting (SC) state [15] and was reported for, e.g., CeRu₂ [16] and UPd₂Al₃ [17]. However, the superconductivity in Yb₃Rh₄Sn₁₃ was shown to be in the dirty limit (i.e., the mean free path is smaller than the coherence length), the strongly pinned region extended up to $0.9T_c$ instead of the expected $0.55T_c$, the Gruenberg-Gunther

parameter is found to be too small (i.e., ~ 0.2 instead of the theoretically calculated 1.8), and finally the acoustically determined PE for $B < B_{c2}$ was by an order of magnitude smaller than that normally observed for a FFLO state [18]. Thus the latter scenario was considered as being rather unlikely.

On the other hand, an anomalous variation in the current density (J_c) across the PE region in Yb₃Rh₄Sn₁₃ together with a slight (by ~ 2 %) temperature softening of the c_{44} mode would disagree with a conventional PE [19]. Further extensive studies based on dc-magnetization and ac-susceptibility measurements revealed a transition from an ordered vortex lattice (VL) [i.e., Bragg glass (BG)] phase to a partially disordered vortex glass (VG)-like phase, which was influenced by an ac driving force [20–23]. The quality of the ordered BG phase in Yb₃Rh₄Sn₁₃ was shown to depend significantly on the crystal orientation (i.e., a better spatially ordered vortex configuration is observed for the magnetic fields applied parallel to the [110] direction) [24]. Small-angle neutron scattering (SANS) revealed hexagonal symmetry of the VL [25] as well as confirmed a phase transition from VL into a glassy phase [26]. These studies indicated the SC state in Yb₃Rh₄Sn₁₃ to be characterized by a stronger electron-phonon coupling together with an isotropically gapped (i.e., *s*-wave) order parameter. All these findings would allow one to assign the Remeika phase (RP) neither to conventional nor to unconventional superconductors.

A situation, where several physical properties of intermetallics crystallizing with the Yb₃Rh₄Sn₁₃ prototype or in structure derivatives remain less clear, is frequently observed [4]. And one of the reasons here is the challenging estimation of the true structural arrangement. Recent studies revealed that such compounds are in many cases charac-

*gumeniuk@physik.tu-freiberg.de

terized by a strong structural disorder [27–29], by ordered superstructures [30–33], by modulations [34], or even by intergrowth on the nanolevel of differently ordered domains [35,36]. Elucidation of these effects is only possible performing combined powder high-resolution synchrotron and single-crystal x-ray diffraction (XRD) together with transmission electron microscopy (TEM) investigations [4]. Such studies suggest that certain Remeika phases do not belong to the class of cage compounds and thus tend toward conventional SC behaviors. For instance, broken time-reversal symmetry (TRS) was reported for the tetragonally distorted RPs $R_5Rh_6Sn_{18}$ ($R = Sc$ [37], Y [38–40], and Lu [40]). However, further studies indicated a strong structural disorder in such phases and consequently s -wave BCS-like superconductivity [41,42] similar to isostructural Ru- and Ir-containing analogs [43–45].

An earlier refinement of the crystal structure of $Yb_3Rh_4Sn_{13}$ indicated unphysical elongation of the thermal ellipsoids for the Sn atoms (at the $24k$ site) in one direction (i.e., $B_{11} \approx 3.5B_{33}$) [46], which could be a signature of both a structural disorder (i.e., splitting of the $24k$ position) and/or of a symmetry lowering. Based on this fact as well as on the puzzling nature of the SC mechanisms for $Yb_3Rh_4Sn_{13}$ we performed a joint investigation of structural, magnetic, thermodynamic, and electrical transport properties. We demonstrate that in $Yb_3Rh_4Sn_{13}$, (i) the crystal structure is disordered; (ii) the lower and upper critical fields are isotropic; (iii) the charge carrier concentration is smaller by a factor of $\approx 10^3$ than those in a simple metal; (iv) a rattling effect manifests itself in both structural refinements and specific heat; (v) superconductivity is in the clean limit and reveals all signatures of a two-gap mechanism.

II. EXPERIMENTAL

Samples of total mass of 1 g and the $Yb_{3+x}Rh_4Sn_{13-x}$ ($x = 0, 0.1, 0.2$) compositions were prepared by high-frequency melting of the mixtures of ytterbium (Ames, 99.95 wt. %), rhodium granules (ChemPur, 99.9 wt. %), and tin foil (ChemPur, 99.995 wt. %) in glassy carbon crucibles. The total weight losses were < 1 wt. %. All sample handling and manipulations were performed inside a glove box system under protective argon atmosphere [$p(H_2O), p(O_2) < 1$ ppm] to avoid oxygen and moisture contamination. The obtained buttons were wrapped in the Mo foil and enclosed in an evacuated silica ampoule. Further, the samples were annealed at 1070 K for 1 month.

In the next step, samples with Yb content $x = 0, 0.1, 0.2$ were placed in separate glassy carbon crucibles together with tin excess in mass proportions 1:15, 1:10, and 1:7, respectively. Then, they were sealed in Nb tubes under Ar atmosphere and enclosed again in evacuated silica ampoules. The crystal growth was performed in programmable muffle furnaces by the following heat treatment profile: heating up to 1370 K within 6 h, staying at this temperature for 6 h, and cooling down to 870 K with 2 K h^{-1} . The Sn excess was removed by centrifugation at 770 K with further washing of the obtained crystals in diluted (1:8) HCl. The largest crystals (i.e., with dimensions up to $5 \times 5 \times 5$ mm) were grown from the synthesis based on the sample with Yb content $x = 0.2$

and Sn excess 1:7. In two other cases smaller specimens (i.e., up to $2 \times 2 \times 2$ mm) were obtained. Interestingly, all crystals revealed almost identical (i.e., peak positions and intensities) powder XRD patterns, indicating them to be of the same composition. This finding is then confirmed not only by structural refinements, but also by coherent physical behaviors, which were measured on three specimens selected from each batch [they are labeled crystal 1 ($x = 0, 1:15$), crystal 2 ($x = 0.1, 1:10$), and crystal 3 ($x = 0.2, 1:7$), respectively].

Differential scanning calorimetry (DSC) measurements performed on synthesized crystals using the Netzsch DSC 404c calorimeter revealed one endothermic effect (Fig. S1 of the Supplemental Material [111]) at 1314 K indicating congruent melting of $Yb_3Rh_4Sn_{13}$.

Powder XRD (PXRD) was performed in transmission mode on a Huber G670 Guinier camera ($CuK_{\alpha 1}$ radiation, $\lambda = 1.54056 \text{ \AA}$, 2θ range 3° – 100° , exposure time 4×30 min). To refine unit cell parameters (UCPs) more precisely, PXRD patterns were measured with LaB_6 ($a = 4.15695 \text{ \AA}$) as an internal standard. Phase analysis was performed with the WinXPow software package [47], whereas Rietveld refinement and calculation of UCPs by the least-squares method were carried out with the WinCSD program package [48].

Single-crystal XRD was performed on a Bruker AXS D8 Quest diffractometer (MoK_{α} , $\lambda = 0.71073 \text{ \AA}$) equipped with a Photon100 detector and a TRIUMPH monochromator [49]. Integration and correction of the obtained data set was done with the APEX software [50]. Crystal structure refinement was performed with WinCSD [48].

One of the crystals was embedded in a conductive resin, ground and polished (final polishing was performed with $0.25 \mu\text{m}$ diamond powder). The obtained surfaces were analysed by scanning electron microscope SEM-JEOL JSM 7800F equipped with a Bruker Quantax 400, XFlash 6||30 (silicon drift detector) energy-dispersive x-ray spectrometer. The composition $Yb_{3.0(1)}Rh_{3.9(1)}Sn_{13.1(1)}$ estimated from this study is in agreement with the refined ones (Table I).

The field and temperature dependent magnetic susceptibility, electrical resistivity, Hall effect, and specific heat capacity for the $Yb_3Rh_4Sn_{13}$ crystals were measured with the VSM, van der Pauw, and HC options, respectively of a DynaCool-12 instrument from Quantum Design. To reach 0.35 K, the ^3He option was used.

The electronic band structure and density of states (DOS) for $Yb_3Rh_4Sn_{13}$ within the local density approximation (LDA) of the density functional theory (DFT) were calculated using the full-potential FPLO code (version 18.00-52.38) [51]. The scalar relativistic calculations were performed using the exchange-correlation potential by Perdew and Wang [52] with the k -mesh of 1728 points in the first Brillouin zone.

III. RESULTS AND DISCUSSION

A. Crystal structure

All peaks in the powder x-ray diffraction (PXRD) patterns of crystals 1, 2, and 3 could be indexed within a cubic primitive lattice with very close (i.e., within two standard deviations) values of the unit cell parameter (UCP) given in Table I, which indicated no homogeneity range for $Yb_3Rh_4Sn_{13}$.

TABLE I. Crystallographic data for Yb₃Rh₄Sn₁₃ [Yb in 6*d* (1/4 0 1/2), Rh in 8*e* (1/4 1/4 1/4), Sn1 in 2*a* (0 0 0)].

Space group (No.)	$Pm\bar{3}n$ (223)
Formula per unit cell, Z	2
Unit cell parameter, ^a a (Å)	9.6709(2)
Unit cell volume, V (Å ³)	904.48(6)
Calculated density, ρ (g cm ⁻³)	9.08(2)
Crystal size (mm ³)	0.02 × 0.06 × 0.11
Absorption coefficient (cm ⁻¹)	371.4
$F(000)$	2080.0
Radiation and wavelength, λ (Å)	MoK α , 0.71073
Temperature (K)	300(2)
Diffractometer	Bruker D8 QUEST
$2\theta_{\max}$ (deg) and $(\sin \theta/\lambda)_{\max}$	72.51 and 0.832
Minimum h, k, l	-16, -16, -16
Maximum h, k, l	16, 16, 16
Absorption correction	multiscan
Collected reflections	96 758
Independent reflections	419 ($R_{\text{int}} = 0.066$)
Refined parameters	20
Reflections with $I_{hkl} \geq 3\sigma(I)$	419 ($R_{\sigma} = 0.0085$)
Refinement on	$ F $
R/wR^b	0.032/0.034
Goodness of fit	1.06
Residual peaks ($e \text{ \AA}^{-3}$)	-0.85; +1.02
Sn2 in 24 <i>k</i> (x 0 z), x, z	0.31567(6), 0.1553(1)
Sn3 in 24 <i>k</i> (x 0 z), x, z	0.29316(7), 0.1508(2)
$G(\text{Sn2}), G(\text{Sn3})$	0.53(1), 0.47(1)
$d(\text{Yb-8Sn2})$ (Å)	3.3585(7)
$d(\text{Yb-4Rh})$ (Å)	3.4192(1)
$d(\text{Rh-6Sn3})$ (Å)	2.6344(5)
$d(\text{Sn1-12Sn3})$ (Å)	3.1882(9)
$d(\text{Sn2-1Sn3})$ (Å)	0.222(1)
$d(\text{Sn2-1Sn3})$ (Å)	2.968(2)
$d(\text{Sn2-2Rh})$ (Å)	2.6622(5)

^aPowder data.^b $w = 1/\ln(F_0)^4$.

Further, one of the crystals from batch 2 was crushed and an appropriate specimen (dimensions are given in Table I) was chosen for single-crystal XRD study. Since the UCP matched those reported in [1], the integration and further refinements

of the collected data were performed within the space group (SG) $Pm\bar{3}n$ (crystallographic details are collected in Table I). Application of direct methods resulted immediately in the structural model found for Yb₃Rh₄Sn₁₃ in [46] and its further refinement (i.e., of extinction-, atomic-, and thermal-displacement parameters) converged with reliability factor $R = 0.076$ and with peaks of the residual electron density (RED) $-3.7/+6.7 e \text{ \AA}^{-3}$. In the next step, the anisotropic displacement parameters (B_{ij}) (Table II) were refined for such a model. This led to the remarkable reduction of the R -factor and RED (i.e., became 0.036 and $-0.84/+1.0 e \text{ \AA}^{-3}$, respectively) as well as to an unphysical B_{11} value of Sn2 (which is nearly twice as large as B_{22} and B_{33}). Such a situation could indicate a split of the 24*k* [$x = 0.3052(1)$, 0 , $z = 0.1532(1)$] (these coordinates were further used for the theoretical DFT calculations) crystallographic position occupied by the Sn2 atom. Here, we would like to refer to our previous work [4], where relations between unphysical anisotropies of thermal displacements and possible crystallographic split positions in Remeika-phase-like structural arrangements are discussed in detail. And indeed, an introduction of a split position occupied by a Sn3 atom (occupational parameter G and refined atomic coordinates are listed in Table I) led to the convergence of the refinement with a lower R factor as well as to reasonable RED (Table I) and B_{ij} values (Table II). Such a structural model (i.e., with a split 24*k* site) is known as Y₃Co₄Ge₁₃ type [53]. The enhanced B_{eq} value for Sn1 (Table II) could also hint toward partial occupancy of the 2*a* position, similarly as reported for the Lu₃Os₄Ge_{13- x} type [54]. However, in the case of Yb₃Rh₄Sn₁₃ this enhancement of the atomic-displacement parameters is ascribed to a rattling effect [55], which is clearly pronounced in the temperature dependence of the specific heat (see discussion below). Further, we used the obtained structural model to perform Rietveld refinement of PXRD data. It converged with reliability factors $R_I = 0.052$ and $R_P = 0.094$ and profiles are presented in Fig. 1, confirming again its correctness.

The shortest interatomic distances in the crystal structure of Yb₃Rh₄Sn₁₃ are collected in Table I. Most of them are by $\approx 4\%$ – 5% longer in comparison with the sums of atomic radii of the elements ($r_{\text{Yb}} = 1.94 \text{ \AA}$, $r_{\text{Rh}} = 1.34 \text{ \AA}$, and $r_{\text{Sn}} = 1.41 \text{ \AA}$ [56]). The exceptions from this observation are

TABLE II. Equivalent (B_{eq})^a and anisotropic (B_{ij}) displacement parameters (in Å²) for Yb₃Rh₄Sn₁₃ refined with and without split position.

Atom	B_{eq}	B_{11}	B_{22}	B_{33}	B_{12}	B_{13}	B_{23}
no split position							
Yb	0.86(1)	0.97(2)	0.80(2)	B_{22}	0	0	0
Rh	0.51(2)	0.51(2)	B_{11}	B_{11}	-0.03(1)	B_{12}	B_{12}
Sn1	1.37(3)	1.37(3)	B_{11}	B_{11}	0	0	0
Sn2	0.98(1)	1.72(2)	0.51(2)	0.70(2)	0	0.25(1)	0
with split position							
Yb	0.85(1)	0.96(2)	0.80(2)	B_{22}	0	0	0
Rh	0.50(1)	0.50(2)	B_{11}	B_{11}	-0.03(1)	B_{12}	B_{12}
Sn1	1.36(2)	1.36(3)	B_{11}	B_{11}	0	0	0
Sn2	0.60(5)	0.65(2)	0.55(5)	0.61(7)	0	0.05(1)	0
Sn3	0.63(6)	0.70(2)	0.58(5)	0.62(8)	0	0.04(2)	0

$$^a B_{\text{eq}} = \frac{1}{3}(B_{11}a^2 + \dots + 2B_{23}b^*c^*bc \cos \alpha).$$

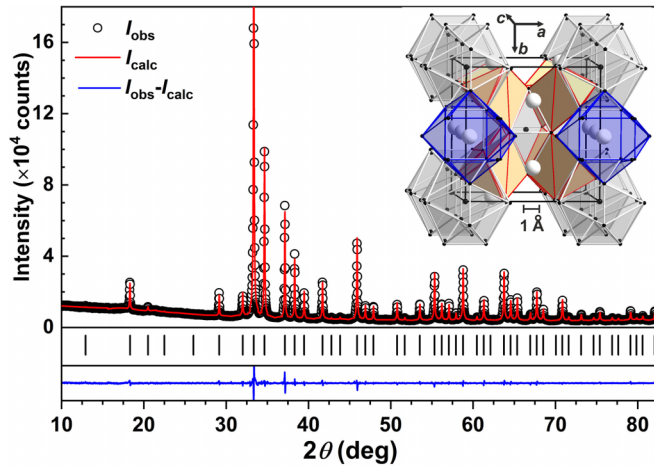


FIG. 1. Powder x-ray diffraction patterns of $\text{Yb}_3\text{Rh}_4\text{Sn}_{13}$. Inset: Arrangement of the $[\text{RhSn}_6]$ trigonal prisms (orange), $[\text{Sn1Sn}_{12}]$ icosahedra (light gray), and $[\text{YbSn}_{12}]$ cuboctahedra (blue) in the crystal structure of $\text{Yb}_3\text{Rh}_4\text{Sn}_{13}$. Yb and Sn atoms are presented as light gray and black balls, respectively.

Yb-Sn2 (is close to the corresponding sum), Rh-Sn3 (is shortened by $\approx 4.2\%$), and the split Sn2-Sn3 contacts. All these variations are typical for intermetallic compounds [57], whereas elongation of the Sn1-Sn3 distance by $\approx 13\%$ (in the case of the refinement without splitting of the $24k$ site this value is even of $\approx 17\%$) would indicate $\text{Yb}_3\text{Rh}_4\text{Sn}_{13}$ to be a cage compound [5,6,11]. This finding is again in agreement with the observed rattling effect due to thermal motion of the Sn1 atom.

The structural relationship of the ideal (i.e., containing no split position) $\text{Yb}_3\text{Rh}_4\text{Sn}_{13}$ Remeika structure type with perovskite and filled skutterudite arrangements is discussed in detail in [4]. This type is described as consisting of an array of corner-sharing $[\text{RhSn}_6]$ trigonal prisms with $[\text{Sn1Sn}_{12}]$ icosahedra and $[\text{YbSn}_{12}]$ cuboctahedra (inset of Fig. 1) embedded therein. Both latter units are again characteristics of a cage compound [5,6,11].

B. Magnetic measurements

The temperature dependencies of magnetic susceptibility $\chi(T)$ of the $\text{Yb}_3\text{Rh}_4\text{Sn}_{13}$ crystals corrected (as proposed in [58]) by diamagnetic increments are plotted in Fig. 2. They are rather small and positive (i.e., reminiscent of weak Pauli paramagnetism [59]) in the whole studied temperature range and thus indicate a domination of the nonmagnetic Yb- $4f^{14}$ state (i.e., Yb^{+2}). The effective magnetic moments of $\approx 1 \mu_B$ estimated from a Curie-Weiss fit of $\chi(T)$ for 250–350 K (not shown in Fig. 2) are in agreement with 20% of Yb^{+3} impurity (i.e., valence state $\nu = 2.2$) reported for $\text{Yb}_3\text{Rh}_4\text{Sn}_{13}$ from XAS investigation [60].

The low-field $\chi(T)$ for a few randomly oriented crystals reveals strong diamagnetic signals (inset to Fig. 2) indicating superconducting transitions with nearly the same (i.e., within a standard deviation) onsets, which are in good agreement with the literature data (Table III). The diamagnetic response in the zero-field cooling (zfc) regime is close to complete in all cases. The differences in the jumps' magni-

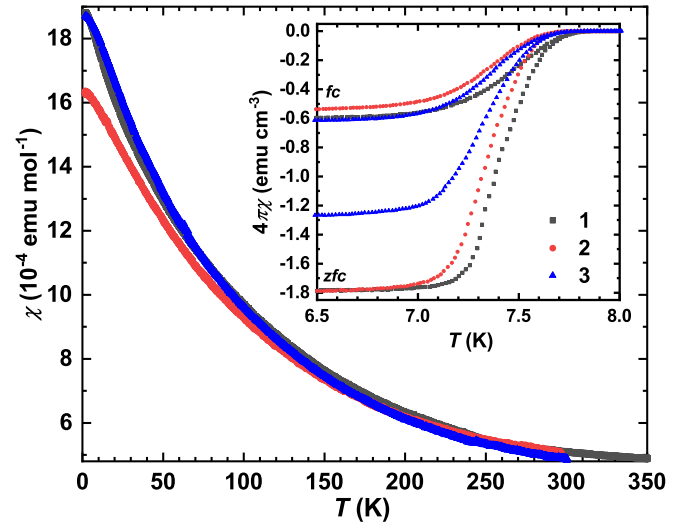


FIG. 2. Magnetic susceptibility of $\text{Yb}_3\text{Rh}_4\text{Sn}_{13}$ crystals for $B = 7$ T and for $B = 2$ mT measured in zfc and fc conditions (inset).

tudes in field-cooled (fc) Meissner effect and zfc curves of the specimens are obviously due to the effect of demagnetizing fields. Indeed, correcting low-field $\chi(T)$ measured in different directions for crystal 3 (the ellipsoidal shape is assumed) as proposed in [61,62] nearly the same (Fig. S2 of the Supplemental Material [111]) fc and zfc jumps were obtained. The differences between them can be explained by imperfections in the synthesized crystals.

Analogously, the different amplitudes of the isothermal magnetization $M(H)$ loops typical for a type-II superconductor became the same while performing correction for demagnetizing factors (cf. Fig. 3(a) and Supplemental Material [111] Fig. S3). Hence, estimating the lower critical fields $[B_{c1}(1.8 \text{ K})]$ for the $[100]$, $[110]$, and $[111]$ directions of crystal 3 as points at which $M(H)$ starts to deviate from linearity the same values are obtained [Fig. 3(b) and Table III]. The obtained here B_{c1} (1.8 K) is somewhat larger than those reported in [13,22,25,26], which can be explained by the fact that the latter were not corrected for demagnetizing fields.

In agreement with the earlier reports, all crystals studied here reveal an unusual hysteretic bubble in both forward $[M(H^+)]$ and reverse $[M(H^-)]$ legs of the $M(H)$ curves prior to the upper critical field (B_{c2}) [Figs. 3(a) and

TABLE III. Superconducting parameters for $\text{Yb}_3\text{Rh}_4\text{Sn}_{13}$ crystals synthesized in this work in comparison with the literature data.

Crystal	T_c^χ/T_c (K)	B_{c1} (T)	λ_L (\AA)	$\kappa(0)$	$B_c(0)$ (mT)
1	7.63(5)				
2	7.58(5)				
3 ^a	7.55(5)	14.5(5)	1790(40)	17(1)	122(1)
[13]	7.8	10.8 ^b	2100	21	110
[22]	7.6	10.0 ^b	2200		
[25]	7.4	8.3(2) ^b	2508(17)	25	
[26]	7.4	13.5	1830 ^b		

^aData measured for $[100]$, $[110]$, $[111]$ directions and corrected for the effect of demagnetizing fields.

^bValues were calculated by us using Eq. (4).

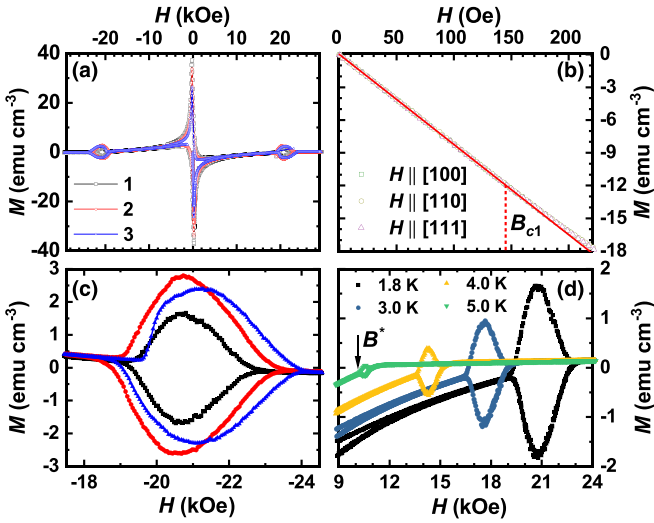


FIG. 3. (a) Magnetization loops for the randomly oriented Yb₃Rh₄Sn₁₃ crystals measured at $T = 1.8$ K. (b) Magnetizations for crystal 3 measured for different directions in low fields and corrected by demagnetizing factors. Deviation from the linearity at the first critical field (B_{c1}) is shown with the dashed line. (c) Peak effect (PE) anomalies in the reversed B^- field for the randomly oriented crystals. (d) Suppression of PE in crystal 1 with increasing temperature. B^* is the field at which the hysteretic peak closes.

3(c)]. This so-called peak effect (PE) phenomenon is well known for Yb₃Rh₄Sn₁₃ and is discussed in the literature [13,14,20,23,24]. It is appearing due to unusual increase in the critical current density $j_c(B)$ and is found to be strongly orientation dependent [24]. The latter fact explains also different amplitudes as well as the onset field positions (B^*) in the studied crystals (Fig. 3(c) and Supplemental Material [111] Fig. S3). PE is suppressed with increasing temperature [Fig. 3(d)] and thus B^* reveals a clear T dependence (see discussion below).

C. Electrical transport

The temperature dependence of electrical resistivity $\rho(T)$ for Yb₃Rh₄Sn₁₃ (crystal 2) is presented in Fig. 4. It decreases with decreasing temperature as expected for a simple metal; however, at the same time, it is nearly by one order of magnitude higher than those of a typical metallic system [59]. Interestingly, at room temperature, $\rho(T)$ is also by a factor of ≈ 5 or ≈ 15 larger compared with the data obtained for Yb₃Rh₄Sn₁₃ in [63] and [25], respectively. Actually, such an excellent conductivity (in accordance with [63] and [25] it is comparable with stainless steel [59]) is rather rare for Remeika phases (for now observed only for Yb₃Co₄Ge₁₃ [34], Sc₅Rh₆Sn₁₈ [64], and U₃Rh₄Ge₁₃ [33]). The latter are normally revealing $\rho(T)$ comparable with RT values of, e.g., La₃Rh₄Sn₁₃, Ce₃Rh₄Sn₁₃ [65], Y₃Rh₄Ge₁₃ [35], Th₃Ir₄Ge₁₃ [28], etc.) or even by a factor of ≈ 2 –4 higher and simultaneously characterized by, for a metal, an unusual increase with decreasing temperature (e.g., Y_{3,4}Rh₄Ge_{12,6} [35], Y₅Ir₆Sn₁₈ [36], Y₅Rh₆Sn₁₈ [39], Lu₅Rh₆Sn₁₈ [41], etc.).

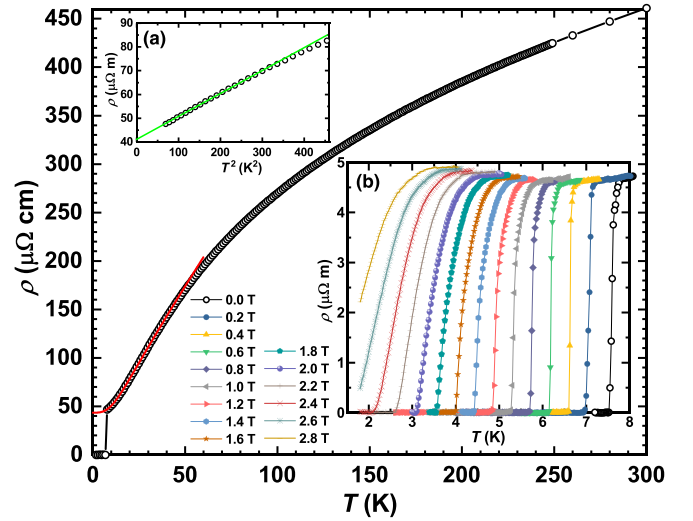


FIG. 4. Temperature dependence of electrical resistivity $\rho(T)$ for Yb₃Rh₄Sn₁₃ (crystal 2). Inset a: Dependence of electrical resistivity from T^2 . Green line shows fit to $\rho_0 + A_{FL}T^2$. Inset b: $\rho(T)$ near the superconducting transition in different magnetic fields.

In the temperature range 8–40 K, $\rho(T)$ of Yb₃Rh₄Sn₁₃ fits well to the Bloch-Grüneisen formula [Eq. (1)] [66]:

$$\rho(T) = \rho_0 + A \left(\frac{T}{\Theta_D^{\text{res}}} \right)^n \int_0^{\Theta_D^{\text{res}}/T} \frac{x^n}{(e^x - 1)(1 - e^{-x})} dx \quad (1)$$

with $n = 3$ (indicating domination of the s – d interband scattering in agreement with a strong relevance of electron-electron scattering due to $\rho \sim T^2$ behavior, as discussed below), the residual resistivity $\rho_0 = 43.4(1) \mu\Omega \text{ cm}$ (stays for the scattering on defects), $A = 1.42(1) \mu\Omega \text{ cm}$ (coefficient depending on the phonon contribution), and Debye temperature $\Theta_D^{\text{res}} = 74(1) \text{ K}$. The latter value is by a factor of ≈ 2.7 smaller than $\Theta_D(0)$ obtained from specific heat and by the same factor larger than the observed Einstein temperature Θ_E (see discussions below). This could indicate that electron scattering in Yb₃Rh₄Sn₁₃ occurs mainly on, e.g., longitudinal acoustic phonons [67]. The residual resistance value (RRR) estimated as ρ_{300}/ρ_0 is found to be 10.6 (compare RRR = 8 reported in [63]) and indicates a good quality of the studied sample.

In the temperature range 7.8–18.8 K, $\rho(T)$ of Yb₃Rh₄Sn₁₃ reveals a quadratic behavior (inset a to Fig. 4) and fits to $\rho_0 + A_{FL}T^2$ with $\rho_0 = 41.2(1) \mu\Omega \text{ cm}$ and $A_{FL} = 9.6(1) \times 10^{-2} \mu\Omega \text{ cm K}^{-2}$. Hence, the Kadowaki-Woods ratio [68] $A_{FL}/\gamma^2 = 1.83 \times 10^{-5} \mu\Omega \text{ cm (mol K)}^2 \text{ mJ}^{-2}$ is calculated. This value is close to $1 \times 10^{-5} \mu\Omega \text{ cm (mol K)}^2 \text{ mJ}^{-2}$, which indicates Yb₃Rh₄Sn₁₃ to be a Fermi liquid system [69].

The Remeika prototype stannide reveals a strong temperature- and magnetic-field-dependent Hall coefficient $R_H(T)$. As one can see from Fig. 5, it decreases upon increasing temperature and becomes larger in higher fields. The latter dependence [i.e., $R_H(B)$] shows also a clear tendency toward saturation, which is especially well pronounced at lower temperatures (Fig. S4 of the Supplemental Material [111]). Strong changes of R_H with T and B have been also observed for numerous isostructural Remeika phases (e.g., Ce₃Rh₄Sn₁₃

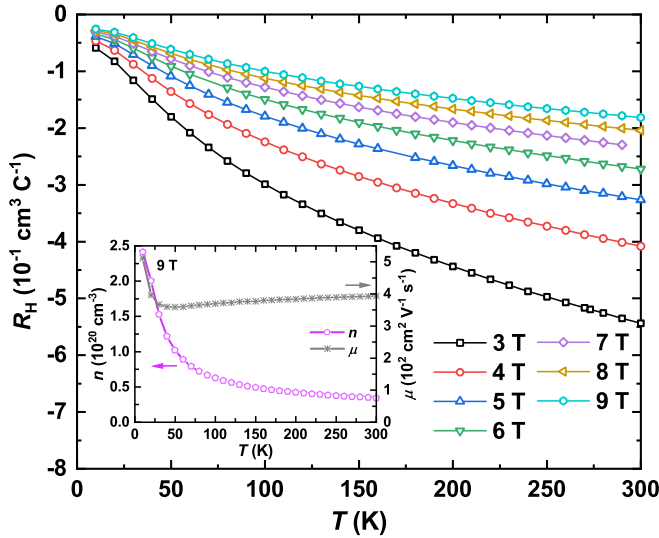


FIG. 5. Temperature dependencies of the Hall coefficient $R_H(T)$ for $\text{Yb}_3\text{Rh}_4\text{Sn}_{13}$ in different magnetic fields. Inset: Temperature dependence of charge carrier concentration $n(T)$ and mobility $\mu(T)$ for $\text{Yb}_3\text{Rh}_4\text{Sn}_{13}$ in a magnetic field $B = 9$ T.

[70], $\text{U}_3\text{Rh}_4\text{Sn}_{13}$ [71], $\text{La}_3\text{Ir}_4\text{Sn}_{13}$ [72], $\text{La}_3\text{Co}_4\text{Sn}_{13}$ [73], $\text{Y}_3\text{Ru}_4\text{Ge}_{13}$ [74], etc.). In all these cases deviation from the behavior of a single-band metal (R_H is expected to be temperature independent [59]) is ascribed to complex band and electronic structures. These are also found to be characteristic for $\text{Yb}_3\text{Rh}_4\text{Sn}_{13}$: nine bands are crossing the Fermi level (E_F) in this stannide (see below).

Interestingly, contrary to the aforementioned compounds, $R_H(T)$ of $\text{Yb}_3\text{Rh}_4\text{Sn}_{13}$ is negative, which indicates an electron-like conduction mechanism. Comparing this result with chemically closely related $\text{Ce}_3\text{Rh}_4\text{Sn}_{13}$ [70] and $\text{U}_3\text{Rh}_4\text{Sn}_{13}$ [71], where conductivity is found to be hole-mediated [i.e., positive values of $R_H(T)$], one could conclude that the type of the latter is defined by the valence balance (i.e., Ce^{+3} and U^{+3} vs Yb^{+2}). And indeed, In-doping of $\text{La}_3\text{Co}_4\text{Sn}_{13}$ (i.e., replacement of Sn^{+4} by In^{+3}) results in $R_H(T)$ behavior, which is almost identical with those in Fig. 5 (cf. Fig. 3(b) of [73]).

Absolute values of $|R_H(T)|$ in the whole studied temperature range for $\text{Yb}_3\text{Rh}_4\text{Sn}_{13}$ are of the same order of magnitude (i.e., $\sim 10^{-1} \text{ cm}^3 \text{ C}^{-1}$) as those of $\text{La}_3\text{Co}_4\text{Sn}_{13}$ [73], $\text{Y}_3\text{Ru}_4\text{Ge}_{13}$ [74], and $\text{Y}_5\text{Ir}_6\text{Sn}_{18}$ [36], thus indicating by a factor of $\sim 10^3$ lower charge carrier concentration $n(T)$ [deduced from $|R_H| = (ne)^{-1}$] (inset of Fig. 5) compared to a conventional metal [59]. Here it should be noted that the change of $n(T)$ by one order of magnitude in the narrow temperature range of 10–130 K (similar behavior is reported for $\text{Y}_3\text{Ru}_4\text{Ge}_{13}$ [74]) is rather artificial due to application of the simplified one-band model. Obviously, the reliable $n(T)$ values are obtained for $T > 130$ K, where the free electron gas model starts to work (see discussion below). Nevertheless, despite all disadvantages of the used model, lowered charge carrier concentration explains well the enhanced electrical resistivity of $\text{Yb}_3\text{Rh}_4\text{Sn}_{13}$. Also, a decrease of n with increasing T accompanied by the temperature-independent charge carrier mobility (calculated from $\mu = |R_H/\rho|$), which

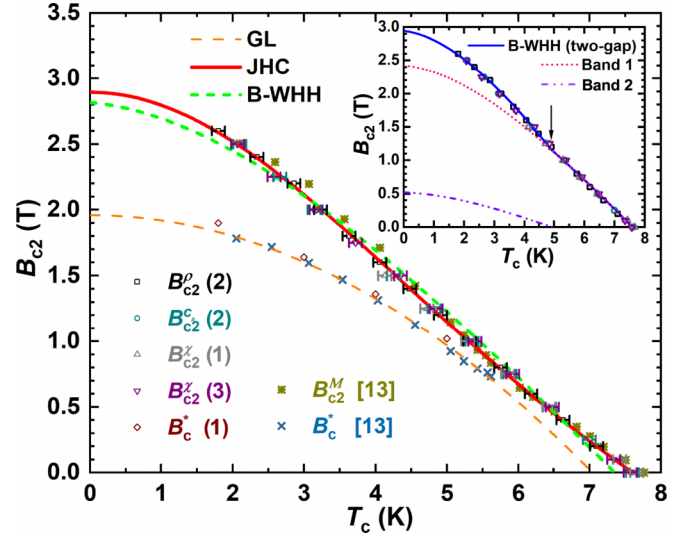


FIG. 6. Upper critical (B_{c2}) and onset (B^*) fields of PE for different $\text{Yb}_3\text{Rh}_4\text{Sn}_{13}$ crystals as a function of critical temperature determined from the electrical resistivity (B_{c2}^ρ), magnetic susceptibility (B_{c2}^χ), and specific heat ($B_{c2}^{\rho p}$) measurements together with the fits to GL-, JHC- and B-WHH models (for more details see text). Inset: Fit of the $B_{c2}(T_c)$ dependence assuming two B-WHH-like bands.

is found to be comparable with those of a simple metal [59] (i.e., $\sim 10^{-2} \text{ cm}^2 \text{ V}^{-1} \text{ s}^{-1}$), are in line with the observed increase of electrical resistivity in the whole studied T range (Fig. 4).

D. Upper critical field

In the inset b to Fig. 4, $\rho(T)$ in various magnetic fields is depicted. The onset of the superconducting transition in zero field is observed at $T_c^{\rho, \text{onset}} = 7.60(5)$ K in good agreement with the values of T_c^{χ} presented in Table III. Further, we plot the upper critical fields (B_{c2}) as well as onset fields B^* of PE determined from diverse measurements for different randomly oriented crystals synthesized in this work together with the literature data [13] as a function of transition temperatures T_c . As one can see from Fig. 6 they follow the same dependence, which brings us to the conclusion that B_{c2} is isotropic and/or independent of the routes of syntheses.

$$B_{c2}(T) = \frac{B_{c2}(0)}{0.697} \left[\left(1 - \frac{T}{T_c} \right) - \left[0.153 \left(1 - \frac{T}{T_c} \right)^2 - 0.152 \left(1 - \frac{T}{T_c} \right)^4 \right] \right] \quad (2)$$

In the next step, we tried to describe the $B_{c2}(T_c)$ dependence with the analytical expression of Baumgartner *et al.* [75], which reproduces the shape of the Werthamer-Helfand-Hohenberg (B-WHH) model [76] [Eq. (2)] and is expected to work in the case of a conventional BCS-like superconductor. However, as one can see from Fig. 6, the B-WHH-fit did not work in the lower and in the middle T_c ranges mainly due the change of the slope, which starts to become steeper at $T_s \approx 5$ K before it saturates. Therefore, we assumed the possible suppression of a small SC gap at T_s (indicated by

an arrow in the inset to Fig. 6) and tried to fit the $B_{c2}(T_c)$ dependence with a sum of two Eq. (2) (i.e., for temperature ranges $T < T_s$ and $T > T_s$, respectively). The total fit to such a model with both contributions is depicted in the inset to Fig. 6. A nice description with the value of the upper critical field $B_{c2}(0) = 2.95(5)$ T could let us to conclude on the two-gap-like SC mechanism in Yb₃Rh₄Sn₁₃. However, as one can see from Fig. 6, the Jones-Hulm-Chandrasekhar (JHC) model [77] [Eq. (3)] provides an excellent description of $B_{c2}(T_c)$ in the whole temperature range and results in a very close value of $B_{c2}(0) = 2.89(5)$ T.

$$B_{c2}(T) = B_{c2}(0) \left[\frac{1 - \left(\frac{T}{T_c}\right)^2}{1 + \left(\frac{T}{T_c}\right)^2} \right] \quad (3)$$

Such cases where temperature dependence of the upper critical fields fits well to several models are also known in the literature (e.g., [78]). This indicates that analysis based only on $B_{c2}(T_c)$ dependence is frequently insufficient to estimate the SC mechanisms in a material and further studies are required.

The B_{c2} values obtained here are by ≈ 0.2 – 0.4 T higher than those from the earlier studies [13,23,25,26]. This could be explained by the fact that in none of the previous works a model analysis was applied to estimate the upper critical field. Taking into account that data from [13] and from [25] (not shown in Fig. 6) agree well with ours, we conclude that B_{c2} values derived in this study are reliable.

Further, using $B_{c2} = \Phi_0/2\pi\xi_{GL}^2$ (where $\Phi_0 = h/2e$ is the flux quantum), the Ginzburg-Landau (GL) coherence length $\xi_{GL}(0) = 107(1)$ Å is calculated. Having this value, we estimated the London penetration depths $\lambda_L(0)$ by the numerical solution of Eq. (4) [79] as well as GL parameters and the thermodynamic critical fields from $\kappa(0) = \lambda_L/\xi_{GL}$ and $B_c(0) = [B_{c1}B_{c2}/\ln(\kappa)]^{1/2}$, respectively. Obtained data are collected in Table III. Importantly, the Ginzburg-Landau parameter is well above $1/\sqrt{2}$, which is in agreement with the type-II superconductivity in Yb₃Rh₄Sn₁₃.

$$B_{c1} = \left(\frac{\Phi_0}{4\pi\lambda_L^2} \right) \ln \left(\frac{\lambda_L}{\xi_{GL}} \right) \quad (4)$$

In this work we pay less attention to the PE in Yb₃Rh₄Sn₁₃, since it was already extensively investigated and the main results on this issue are collected in [13,23,24]. In Fig. 6 we compare the temperature evolution of B^* (the field at which the hysteretic bubble due to PE closes) of our sample with the data from [13]. Interestingly, both of them fit well to the Ginzburg-Landau (GL) equation [Eq. (5)]:

$$B^* = B^*(0) \left[1 - \left(\frac{T}{T_c^*}\right)^2 \right] \quad (5)$$

with $B^*(0) = 1.96(9)$ T and $T_c^* = 7.1(1)$ K $\approx 0.93T_c$ in agreement with other studies [13,14].

E. Specific heat

The suppression of the steplike anomaly due to a SC transition in the temperature dependence of the specific heat capacity of Yb₃Rh₄Sn₁₃ (crystal 2) [presented as $c_p/T(T)$]

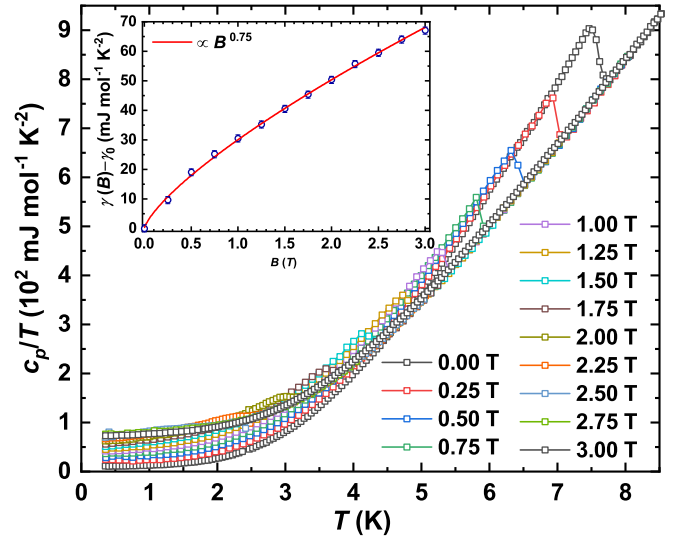


FIG. 7. Specific heat capacity of Yb₃Rh₄Sn₁₃ in different magnetic fields in $c_p/T(T)$ presentation. Inset: Magnetic field dependence of the Sommerfeld coefficient of electronic specific heat for Yb₃Rh₄Sn₁₃ together with a power-law fit to $\propto B^{0.75}$.

with increasing magnetic field is depicted in Fig. 7. No superconductivity became visible down to 0.35 K while reaching $B \geq 2.75$ T.

The $c_p(T)$ dependence for the overcritical field ($B = 3$ T) fits well (inset to Fig. 8) to $ansatz$ $c_p(T) = \gamma_{tot}T + \beta T^3$ with $\gamma_{tot} = 72.5(5)$ mJ mol⁻¹ K⁻² and $\beta = 4.5(5)$ mJ mol⁻¹ K⁻⁴, which corresponds to a Debye temperature $\Theta_D = 232(1)$ K (in fair agreement with $\Theta_D = 195$ K obtained from the measurements of elastic properties [18]). However, this approach works only in a narrow T range of 0.35–2 K. Adding further a δT^5 phononic term with $\delta = 4.3(1) \times 10^{-5}$ J mol⁻¹ K⁻⁶ we could extend this range up to ≈ 4.5 K; however above

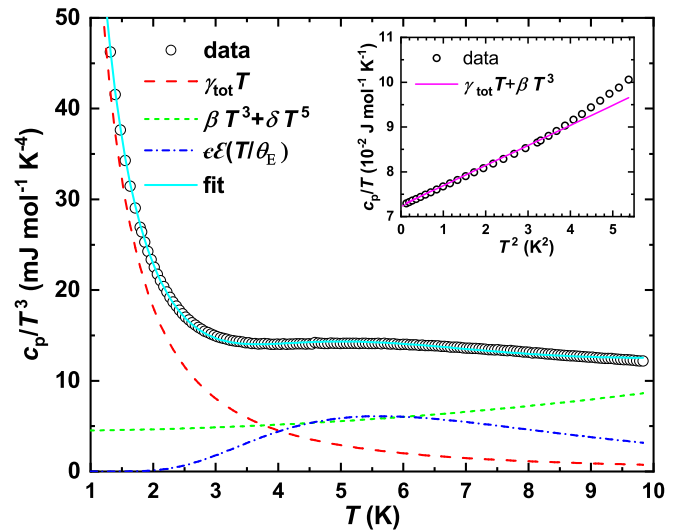


FIG. 8. Specific heat for Yb₃Rh₄Sn₁₃ in overcritical field ($B = 3$ T) in $c_p/T^3(T)$ presentation together with the fit to Eq. (6) and its electronic ($\gamma_{tot}T$), phononic ($\beta T^3 + \delta T^5$), and Einstein [$\epsilon\mathcal{E}(\Theta_E/T)$] contributions. Inset: Low-temperature $c_p(T)$ together with the fit to the Debye ansatz.

this temperature the Debye model fails in the description of $c_p(T)$ of $\text{Yb}_3\text{Rh}_4\text{Sn}_{13}$. Therefore, in the following we tried to take into consideration possible rattling modes, suggested by the crystal structure refinement (Table II). They also manifest themselves in form of a well pronounced maximum centered at ≈ 5.5 K in the $c_p/T^3(T)$ dependence [80,81] (Fig. 8), which can be described by adding of an Einstein-term to the *ansatz* above [80,82,83]:

$$c_p(T) = \gamma_{\text{tot}}T + \beta T^3 + \delta T^5 + \epsilon \mathcal{E}(\Theta_E/T), \quad (6)$$

where $\mathcal{E}(\Theta_E/T)$ is the Einstein function [83] and $\epsilon = 3 R y$ reflects three degrees of freedoms for each rattling atom (i.e., $y = 1$ for Sn1 in our case). To perform the fit to Eq. (6) we fixed γ , β , and δ to the values given above deducing $\epsilon = 6.5(1) \text{ J mol}^{-1} \text{ K}^{-1}$ and $\Theta_E = 28 \text{ K}$. The former value, however, indicates a strongly underestimated number of rattlers (i.e., $y = 0.26$ instead of the expected 1). The structural arrangement of Remeika type hosts a much more complex phonon spectrum than those of heavy atom-filled skutterudites [80,82] or intermetallic clathrates [84], where this simplified model was reasonably well working. Also, recalculating B_{eq} of the rattling Sn1 atom (Table II) into Einstein temperature Θ_E^B using Eq. (7) we obtain 89 K, which is again by a factor of ≈ 3 larger than the value deduced from the specific heat data. Such a discrepancy was also encountered in the case for filled skutterudites, where the atomic mass of the rattler (Ra) was comparable with those of the atoms forming the framework (e.g., $Ra\text{Fe}_4\text{Sb}_{12}$ with $Ra = \text{Na}, \text{Ca}, \text{Sr}$) [82,85].

$$\Theta_E^B = \sqrt{\frac{8\pi^2 \hbar^2 T}{m_{\text{Sn}} k_B B_{\text{eq}}}} \quad (7)$$

Additionally, rattling is known to strongly influence the electronic structure as well as to give rise to an exotic superconducting state characterized by the possible formation of heavy quasiparticles due to off-center degrees of freedom of ions [86,87]. Resulting from it anharmonic phonons are shown to play an important role in the enhancement of electronic specific heat and superconducting transition temperatures (as, e.g., in KOs_2O_6 [87], $\text{LaRu}_4\text{As}_{12}$ [88], etc.). Investigating SC properties of the $MV_2\text{Al}_{20}$ series with $M = \text{Sc}, \text{Y},$ and Lu , the authors of [89] observed a T_c increase while strengthening anharmonicity of the ionic vibrations. Further performed theoretical calculations of the phononic dispersions and density of states (PhDOS) confirmed this trend giving the highest electron-phonon coupling parameter for $\text{ScV}_2\text{Al}_{20}$ ($T_c \sim 1 \text{ K}$), intermediate values for $M = \text{Y}$ and Lu ($T_c \sim 0.6 \text{ K}$), and the smallest for nonsuperconducting $M = \text{La}$. Accordingly, one can assume that a rattling effect in $\text{Yb}_3\text{Rh}_4\text{Sn}_{13}$ is strongly contributing to superconductivity, since this stannide reveals the highest known for now T_c among all studied Remeika phases (cf. Table 4 in [4]). However, more detailed analysis in this respect, as done for the $MV_2\text{Al}_{20}$ series, would be rather complicated, since isostructural $Ra\text{Rh}_4\text{Sn}_{13}$ compounds are either crystallizing in different structure types ($Ra = \text{La}, \text{Ce}$) or their specific heat ($Ra = \text{Ce}, \text{Pr}, \text{Eu}, \text{Gd}$) is affected by magnetic orderings and/or crystal electric field effects [4], making elucidation of rattling motions very challenging. Additionally, simulations

of PhDOS for $\text{Yb}_3\text{Rh}_4\text{Sn}_{13}$ would require special approaches in view of the occurrence of structural disorder due to the split position in its crystal structure and should become an object of a separate study.

In the following $c_p(T)$ of crystal 2 near the SC transition in zero field was analyzed within a graphical equal-areas approximation (entropy-conserving) resulting in critical temperature $T_c^{c_p} = 7.62(1) \text{ K}$ (in good agreement with the values from Table III) and the specific heat jump $\Delta c_p/\gamma_{\text{tot}}T_c = 2.38(1)$. The jump considerably exceeds the prediction of the BCS theory (i.e., 1.43) as well as those earlier reported [13] and thus indicates a strong electron-phonon coupling in the $\text{Yb}_3\text{Rh}_4\text{Sn}_{13}$ superconductor. This finding would be also in agreement with the enhanced (i.e., close to 1) value of the electron-phonon coupling parameter $\lambda_{\text{el-ph}} = 0.82(3)$, which was deduced from the McMillan formula (with the repulsive screened Coulomb potential $\mu^* = 0.13$):

$$\lambda_{\text{el-ph}} = \frac{1.04 + \mu^* \ln(\Theta_D/1.45T_c)}{(1 - 0.62\mu^*) \ln(\Theta_D/1.45T_c) - 1.04}. \quad (8)$$

In a theoretical study [90] Eq. (8) is shown to be valid for two-gap superconductors and is typically applied to estimate $\lambda_{\text{el-ph}}$ in such materials (e.g., ReBe_{22} [91], LaNiC_2 [92], Th_7Fe_3 [93], etc.).

$$\Delta c_p/\gamma_{\text{tot}}T_c = 1.43 \left[1 + 53 \left(\frac{T_c}{\omega_{\text{ln}}} \right)^2 \ln \left(\frac{\omega_{\text{ln}}}{3T_c} \right) \right] \quad (9)$$

$$T_c = 0.715 \omega_{\text{ln}} \frac{(0.507\lambda + 0.0436)^4}{(0.828\lambda + 0.00637)^3 + \sqrt{1.85\mu^* - 0.00743}} \quad (10)$$

An additional approach allowing estimation of the coupling parameter and based on the different to McMillan consideration of electron-phonon interactions appearing in the Eliashberg theory is proposed by Allen and Dynes [94]. Calculating the logarithmic averaged phonon frequency $\omega_{\text{ln}} = 167.43$ using Eq. (9) [95] and applying it together with the above given value of the repulsive screened Coulomb potential in Eq. (10) (Allen-Dynes formula improved by machine-learning algorithm [96]), we deduce the electron-phonon coupling parameter $\lambda = 0.84(2)$ in excellent agreement with the above obtained $\lambda_{\text{el-ph}}$.

Further, the temperature dependence of the electronic specific heat (c_{el}) (obtained after subtraction of Debye and Einstein contributions) of $\text{Yb}_3\text{Rh}_4\text{Sn}_{13}$ (Fig. 9) in zero field is analyzed. It seems to be nearly comparable to the α model assuming a stronger electron-phonon coupling with $\alpha \equiv \Delta(0)/k_B T_c = 2.3 > \alpha_{\text{BCS}} = 1.764$ [97]. This finding would acceptably agree with the energy-gap ratio of 2.8 deduced from a small-angle neutron scattering (SANS) study [25]. However, presenting normalized $c_{\text{el}}/\gamma T_c$ electronic specific heat in semilog scale against reciprocal temperature T_c/T (inset of Fig. 9), one can see that it is linear [i.e., compatible with α -model and simple s -wave BCS-like $\propto \exp(-\Delta/k_B T_c)$ behavior] in the very narrow T_c/T ranges. On the other hand, linearity in this dependence at higher T_c/T values followed by a strong upturn while reducing them is a typical feature for a two-gap superconductor, which is reported in such state-of-the-art materials as $\text{Lu}_2\text{Fe}_3\text{Si}_5$ [98] and $\text{YNi}_2\text{B}_2\text{C}$ [99].

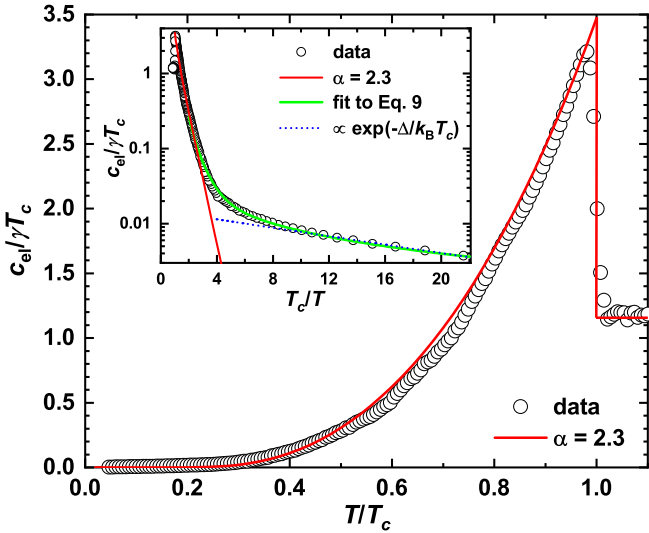


FIG. 9. Temperature dependence of the electronic specific heat for Yb₃Rh₄Sn₁₃ in comparison with the α model [97]. Inset: A semilog graph of electronic specific heat against T_c/T together with α -model, $\propto \exp(-\Delta/k_B T_c)$ approximation, and the fit to Eq. (11) for $T < T_c/2$ K.

Therefore, c_{el} of Yb₃Rh₄Sn₁₃ was further fitted to Eq. (11) for $T < T_c/2$ (inset of Fig. 9):

$$c_{el} = \gamma_0 T + \gamma_{tot} T_c [xA_1 e^{-\Delta_1/k_B T} + (1-x)A_2 e^{-\Delta_2/k_B T}]. \quad (11)$$

It converged with $\gamma_0 = 5.8(1)$ mJ mol⁻¹ K⁻², $x = 0.87(1)$, $A_1 = 57(1)$, $\Delta_1/k_B T_c = 3.52(1)$ (which is in acceptable agreement with the order parameter calculated from the Ginzburg-Landau coherence length, i.e., $\Delta_0/k_B T_c = 4.08$; see discussion below), $A_2 = 27(1)$, and $\Delta_2/k_B T_c = 1.32(1)$. This indicates that the larger (i.e., of 87%) gap Δ_1 obeying an exponential function is still s -wave, despite being characterized by an extremely strong electron-phonon coupling. On the other hand, the smaller (i.e., of 13%) gap Δ_2 is somewhat smaller than the BCS prediction [i.e., $\Delta(0)/k_B T_c = 1.764$] in agreement with earlier reports for two-gap superconductors [83,98–101]). Two-gap superconductivity in Yb₃Rh₄Sn₁₃ would be also in agreement with the power-law-like $\gamma_B \propto B^n$ ($n = 0.75$) dependence (inset of Fig. 7). Such a SC mechanism has been recently reported for the Y₃Ru₄Ge₁₃ [102] and Lu₃Ru₄Ge₁₃ [103] Remeika phases. Although several factors hint toward multiband superconductivity in the studied stannide, additional field and temperature dependent thermal conductivity measurements could help to substantiate this scenario. Such a study would be especially important in view [104–106] of the observed complex electronic structure for Yb₃Rh₄Sn₁₃.

In the next step, we corrected the normal state electronic specific heat coefficient (γ_{tot}) by the residual term (γ_0) and obtained $\gamma_N = \gamma_{tot} - \gamma_0 = 66.7(2)$ mJ mol⁻¹ K⁻². The electronic density of states (DOS) at the Fermi level $N(E_F) = 30.76(1)$ states eV⁻¹ f.u.⁻¹ and the bare DOS $N_{band}(E_F) = 28.30(1)$ states eV⁻¹ f.u.⁻¹ deduced from γ_{tot} and γ_N , respectively, strongly deviate from the theoretically obtained $N_{theor}(E_F) = 14.99(1)$ states eV⁻¹ f.u.⁻¹ for the idealized structure. However, recalculating a

Sommerfeld coefficient $\gamma_{bare} = 35.3$ mJ mol⁻¹ K⁻² from the latter value, we could find the electron-phonon coupling parameter $\lambda = (\gamma_N/\gamma_{bare}) - 1 = 0.89$, which is in good agreement with the ones deduced from the McMillan and Allen-Dynes formulas [Eqs. (8) and (10)]. Further, knowing that the DOS at E_F and the effective mass of the quasiparticles m^* depend on the many-body electron-phonon interactions in similar way, i.e., $N(E_F) = N_{band}(E_F)(1 + \lambda_{el-ph})$ and $m^* = m_{band}^*(1 + \lambda_{el-ph})$, and taking into account that $m_{band}^* = m_e$, the mass of the quasiparticles as $m^* = 1.86m_e$ was estimated.

$$\gamma_N = \frac{\pi^2 k_B^2 N_A m_e}{\hbar^2 (3\pi^2 n)^{2/3}} \quad (12)$$

Unexpectedly, from Eq. (12) a charge carrier concentration $n = 5.54 \times 10^{19}$ cm⁻³ is found being the same as the experimental value observed at ≈ 130 K (inset of Fig. 5). This indicates that a simplified free electron gas theory could work in the case of Yb₃Rh₄Sn₁₃, in agreement with the numerous parabolic bands and spherical sheets of the complex Fermi surface calculated for this compound (see below). Taking the charge carrier concentration $n_{10K} = 2.41 \times 10^{20}$ cm⁻³ (experimentally measured at 10 K), a Fermi velocity of $v_F = (\hbar/m)(3\pi^2 n)^{1/3} = 2.23 \times 10^5$ m s⁻¹ and the mean free scattering time $\tau = m^*/\rho_0 n e^2 = 6.49(2) \times 10^{-13}$ s are obtained. Hence, the mean free path $l = v_F \tau = 1447$ Å is calculated. Finally, we find the relation $l/\xi_{GL} = 13.5 \gg 1$ and can conclude that the superconductivity in Yb₃Rh₄Sn₁₃ is in the clean limit.

F. Possible FFLO state

This latter finding is in contradiction with the earlier reports [13,14], where the mean free path is found to be shorter than the coherence length. However, it should be noted that in both these works the charge carrier density was not directly measured, but was assumed to be of the same order of magnitude as of a simple metal (i.e., $\approx 10^{22}$ cm⁻³). The fact that $l < \xi_{GL}$ was also interpreted as one of the reasons why a Fulde-Ferrell-Larkin-Ovchinnikov (FFLO) state in Yb₃Rh₄Sn₁₃ is impossible.

The generalized FFLO state can occur in a superconductor with a greatly enhanced Ginzburg-Landau parameter [i.e., $\kappa(0) \gg 1$] being simultaneously in the clean limit and revealing peak effects [17]. Our study shows Yb₃Rh₄Sn₁₃ to fulfill all these conditions. And even more, the observed $\kappa(0)$ (Table III), $l < \xi_{GL}$ ratio, and $B^*(0)$ are comparable with those of such superconductors in a FFLO state as UPd₂Al₃ and CeRu₂ [16]. In this view, further analysis seemed to be required. Therefore, we calculated for Yb₃Rh₄Sn₁₃ the orbital critical field given as $B_{c2}^{orb} = B_{c2}(e^{2+\gamma_E}/\pi^2) = 3.85$ T ($\gamma_E = 0.57721$ is the Euler constant), which is, in contrast to UPd₂Al₃, much smaller than B_{c2}^P of the Pauli-paramagnetic limit and indicates a strong orbital pair breaking. On the other hand, the paramagnetically limited upper critical field $B_P = \Delta_0/\mu_B \sqrt{2} = 32.7$ T, where $\Delta_0 = \hbar v_F/\pi \xi_{GL} = 2.68$ meV is a SC order parameter [for its calculation, charge carrier concentration obtained from Eq. (12) was used] with much larger value compared to UPd₂Al₃ and CeRu₂ [16]. Hence, the parameter $\beta_G = B_{c2}^{orb} \sqrt{2}/B_P$, proposed by Gruenberg and Gunther [15] and expected to be > 1.8 for a superconductor

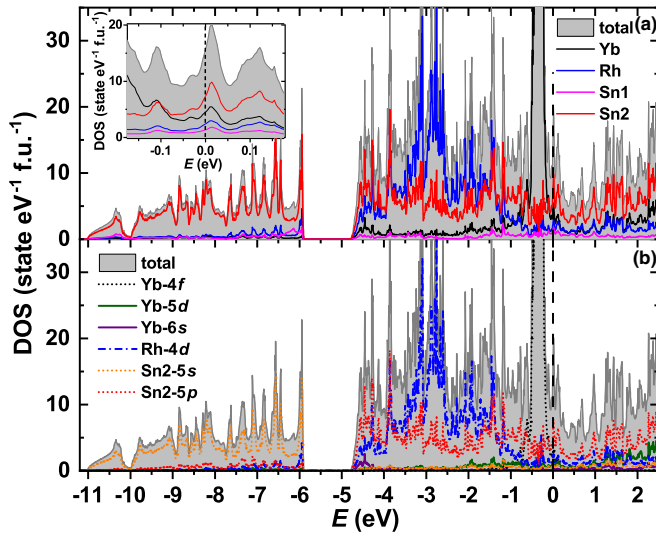


FIG. 10. (a) Total and atomic-resolved electronic density of states (DOS) for $\text{Yb}_3\text{Rh}_4\text{Sn}_{13}$. Inset: DOS near the Fermi level E_F . (b) Total and orbital-resolved DOS.

in FFLO state, is in our case of only 0.17 (it is, e.g., 2.5 and 1.2 for UPd_2Al_3 and CeRu_2 , respectively [16]). Even if the order parameter obtained for the second gap (i.e., $\Delta_2 = 1.1$ eV) were taken into consideration, this would indicate $B_p = 13.1$ T, and thus $\beta_G = 0.42$, still well below the theoretical expectation. Therefore, the occurrence of a generalized FFLO state in $\text{Yb}_3\text{Rh}_4\text{Sn}_{13}$ is rather unlikely.

G. Electronic band structure

The electronic density of states (DOS) calculated for the structural model of $\text{Yb}_3\text{Rh}_4\text{Sn}_{13}$ without split position is presented in Fig. 10(a). The valence band in such an electronic structure is characterized by a low-lying energy region (extends from ~ -11 eV to ~ -6 eV) separated from the higher-lying one [~ -5 eV to Fermi level (E_F)] by an energy gap of ≈ 1 eV. The Fermi level is situated on the slope of the DOS [inset of Fig. 10(a)], which would indicate an instability of $\text{Yb}_3\text{Rh}_4\text{Sn}_{13}$ with any electron-hole doping and thus explain the absence of (i) a homogeneity range for this compound as well as (ii) formation of the isostructural stanides with the neighboring rare-earth atoms (R) (i.e., R -Rh-Sn systems, where $R = \text{Tb}, \text{Dy}, \text{Ho}, \text{Er}, \text{Tm}$ are characterized by the tetragonal arrangements with the close 5:6:18 compositions [1]). Similar to recently reported superconducting Remeika phases [31,35,36,64] and structurally related filled skutterudites [9,10,107], the Fermi level in $\text{Yb}_3\text{Rh}_4\text{Sn}_{13}$ is mainly populated by p states of the p -element (i.e., contributions from Sn atoms are of $\approx 56\%$), whereas the states of d -transition metals are much less present (i.e., we observe only $\approx 15\%$ of Rh-4d at E_F).

The orbitally resolved DOS for $\text{Yb}_3\text{Rh}_4\text{Sn}_{13}$ is depicted in Fig. 10(b). The Yb-4f states are almost completely below the E_F and form a narrow peak centered at ≈ -0.35 eV, which would indicate them to be fully populated, whereas Yb-5d and Yb-6s are above the Fermi level and, thus, empty. These observations would support a +2 oxidation state of Yb in line with the experimental findings. The Rh-4d and Sn2-5p bands

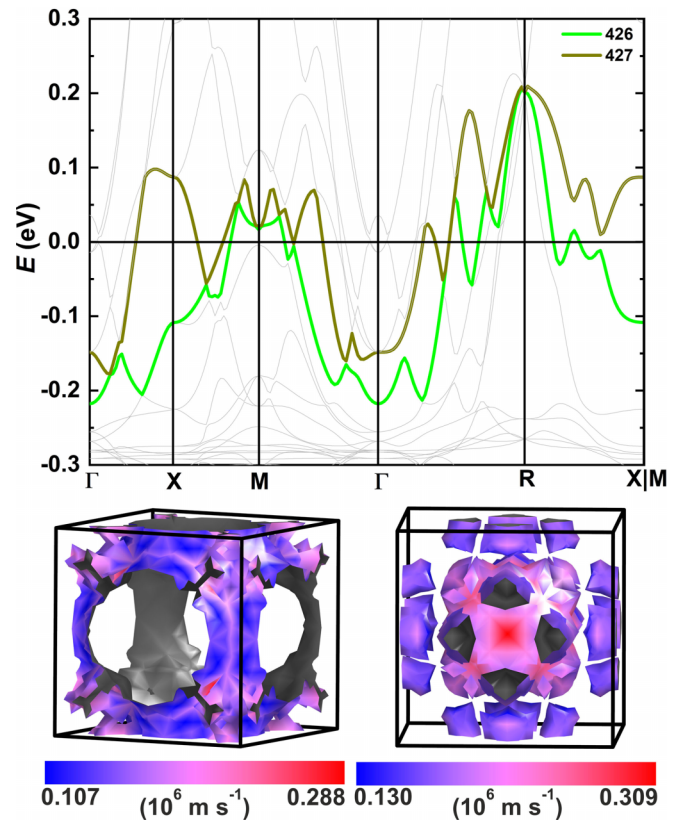


FIG. 11. Band structure of $\text{Yb}_3\text{Rh}_4\text{Sn}_{13}$ in close vicinity to E_F together with the calculated hole-like (band 426) (left) and electron-like (band 427) (right) Fermi surfaces. The lower scale represents the distribution of Fermi velocities.

form the broad upper energy band ($E > -5$ eV), whereas the lower one ($E < -6$ eV) is mainly due to Sn2-5s electrons. Thus, the contribution of the latter to the superconductivity in $\text{Yb}_3\text{Rh}_4\text{Sn}_{13}$ is rather unlikely.

The electronic band structure for $\text{Yb}_3\text{Rh}_4\text{Sn}_{13}$ near the Fermi level together with the calculated Fermi surfaces (FSs) are presented in Fig. 11 and Supplemental Material [111] Fig. S5. The former is very complex, since nine bands are found to cross E_F . Seven of them are nearly parabolic and are located mainly either at the Γ point (i.e., bands 428–431) or at the R point (i.e., bands 423–425) (Fig. S5 of the Supplemental Material [111]). Therefore, the corresponding FSs are either embedded in each other's bowed spheres with pointed vertices centered in the first Brillouin zone (for the bands 428–431) or open pockets at the apexes of the latter (i.e., bands 423–425). Interestingly, bands 426 and 427 cross E_F at many points and thus reveal hole-like (426) and electron-like (427) Fermi surfaces of much more complex character (Fig. 11). Such a band structure strongly deviates from the classical ones (i.e., with 2–3 bands at E_F) observed for the state-of-the-art two-gap superconductors (e.g., MgB_2 [108], $\text{Lu}_2\text{Fe}_3\text{Si}_5$ [98], or AgMo_6S_8 [109]). However, on the other hand, this SC scenario is also reported for numerous compounds where multiple bands are crossing the Fermi level. For instance, these are $\text{YNi}_2\text{B}_2\text{C}$ [110] and ReBe_{22} [91]. Interestingly, the electronic band structure of the latter beryllide is found to be characterized by a much larger size of the electron pockets

centered around the Γ point in comparison with the hole-like ones near the L point, which is shown to be one of the reasons for the two-gap superconductivity. The difference in the sizes of the bands around the Γ and R points in Yb₃Rh₄Sn₁₃ is less pronounced in comparison to those in ReBe₂₂ (cf. Fig. S5 of the Supplemental Material [111] and Fig. 12 of [91]); nevertheless it is clearly visible, especially in the corresponding Fermi surfaces (Fig. S5 of the Supplemental Material [111]). Additionally, the cylindrical hole-like FSs in MgB₂ are reminiscent of those shown in Fig. 11 for the band 426 (cf. Fig. 3 of [108]). However, despite showing some similarities with the known two-gap superconductors, the band structure of Yb₃Rh₄Sn₁₃ needs additional experimental proofs (e.g., by de Haas–van Alphen, ARPES, etc., methods) especially in view of its crystal structure with a split crystallographic position.

IV. CONCLUSIONS

Indexing of the powder x-ray diffraction (PXRD) patterns of the samples with Yb_{3+x}Rh₄Sn_{13-x} ($x = 0, 0.1, 0.2$) compositions indicated them to crystallize with a primitive cubic (space group $Pm\bar{3}n$) structure with identical unit cell parameters, thus revealing no homogeneity range. Further, large single crystals were synthesized from these specimens by the Sn-flux method. PXRD and measurements of physical properties showed them to be of the same Yb₃Rh₄Sn₁₃ composition. Structural refinements performed on powder and single-crystal XRD data revealed the Remeika phase to crystallize with primitive cubic (space group $Pm\bar{3}n$) disordered Y₃Co₄Ge₁₃ structure type characterized by the split of the 24k Wyckoff position occupied by Sn2 atoms. Enhanced thermal-displacement parameters for Sn1 at the 2a site (i.e., centering an enlarged icosahedron) indicate rattling-like movements of this atom.

The temperature dependence of magnetic susceptibility of Yb₃Rh₄Sn₁₃ is found to be reminiscent of a Pauli paramagnet in agreement with a previous XAS study reporting domination of the nonmagnetic Yb-4f¹⁴ state. At the critical temperature $T_c^X = 7.63(5)$ K a strong diamagnetic signal confirms a transition into a superconducting (SC) state. No anisotropy for T_c and the lower B_{c1} and upper $B_{c2}(0)$ critical fields is observed. Another characteristic feature observed for Yb₃Rh₄Sn₁₃ in both legs of $M(H)$ prior to B_{c2} is the so-called peak effect (PE): a hysteretic bubble with the onset field position B^* appearing due to an unusual increase in the critical current density $j_c(B)$. Being strongly orientation dependent it reveals different amplitudes as well as B^* . PE is suppressed with increasing temperature.

To obtain the $B_{c2}(0)$ and $B^*(0)$ values measurements of magnetic susceptibility, electrical resistivity, and specific heat capacity at different temperatures and magnetic fields were performed. $B_{c2}(T_c)$ and $B^*(T_c)$ dependencies could be modeled by the sum of two Werthamer-Helfand-Hohenberg equations from Baumgartner (B-WHH), Jones-Hulm-Chandrasekhar (JHC), or Ginzburg-Landau (GL) models, respectively, resulting in $B_{c2}(0) = 2.89(5)$ T and $B^*(0) = 1.96(9)$ T. The fact that $B_{c2}(T_c)$ reveals

a complex behavior already suggested a multiband SC mechanism.

Electrical resistivity of Yb₃Rh₄Sn₁₃ above T_c is by 1–2 orders of magnitude higher than those expected for a simple metal. This observation is in line with a lowered charge carrier concentration (i.e., $n \sim 10^{19-20}$ cm⁻³), which was deduced from Hall effect measurements. The latter revealed also a strong temperature and field variation reflecting the complex electronic band structure of the studied stannide. Its charge carrier mobility is found to be temperature independent and comparable to a metallic-like one.

The temperature dependence of the specific heat of Yb₃Rh₄Sn₁₃ in overcritical field could be described only by a combined Debye-Einstein model, which indicated a complex phononic spectrum and a well-pronounced rattling effect. Further, the calculated specific heat jump $\Delta c_p / \gamma_{\text{tot}} T_c = 2.38(1)$ is well above the BCS prediction (i.e., 1.43) and in agreement with the enhanced values of the $\lambda_{\text{el-ph}} = 0.82(3)$ (or 0.89) parameter indicating a strong electron-phonon coupling in the studied superconductor. Below T_c the electronic specific heat, obtained after subtraction of the Debye and Einstein phononic contributions, could be described only assuming a two-band model with gap ratios $\Delta_1 / k_B T_c = 3.52(1)$ and $\Delta_2 / k_B T_c = 1.32(1)$ and respective weights of 87(1)% and 13(1)%. This finding agrees also well with the power-law-like $\gamma(B) \propto B^{0.75}$ dependence. Unexpectedly, based on a simplified free-electron gas model a reasonable value for the charge carrier concentration in Yb₃Rh₄Sn₁₃ was calculated. So, the mean free path $l = 1447$ Å was estimated. With this value and the GL coherence length [$\xi_{\text{GL}}(0) = 107(1)$ Å] their ratio $l / \xi_{\text{GL}} = 13.5 \gg 1$ indicates superconductivity to be in the clean limit. We have also shown that occurrence of the generalized Fulde-Ferrell-Larkin-Ovchinnikov (FFLO) state in the studied stannide is rather unlikely.

The electronic band structure (EBS) and density of states (DOS) were obtained for the idealized Yb₃Rh₄Sn₁₃ structure (i.e., with no split position) within the density functional theory (DFT). They indicate a significantly smaller DOS at the Fermi level (E_F) in comparison with those deduced from experiment indicative of a strong electron-phonon coupling as well as a complex EBS with nine bands crossing E_F . Seven of them are nearly parabolic, and the electronic pockets centered around the Γ point reveal some differences in size with the hole-like bands at the R point. This finding, together with the fact that the hole-like band 426 shows a cylindrical Fermi surface, supports a two-gap SC mechanism in Yb₃Rh₄Sn₁₃.

ACKNOWLEDGMENTS

The authors thank H. Borrmann for performing powder XRD, S. Scharsach for DSC measurements, and M. Feig for his support in the initial stage of this work. We are also grateful to Y. Grin for his interest in this work. The physical property measurements in this work were performed on the DynaCool-12 system acquired within the Deutsche Forschungsgemeinschaft (DFG) Project No. 422219907. V.L. thanks DFG for financial support (Project No. 467257848).

- [1] J. Remeika, G. Espinosa, A. Cooper, H. Barz, J. Rowell, D. McWhan, J. Vandenberg, D. Moncton, Z. Fisk, L. Woolf, H. Hamaker, M. Maple, G. Shirane, and W. Thomlinson, A new family of ternary intermetallic superconducting/magnetic stannides, *Solid State Commun.* **34**, 923 (1980).
- [2] T. Barth, Die Kristallstruktur von Perowskit und Verwandten Verbindungen, *Nor. J. Geol.* **8**, 201 (1925).
- [3] W. Jeitschko and D. Braun, $\text{LaFe}_4\text{P}_{12}$ with filled CoAs_3 -type structure and isotypic lanthanoid-transition metal polyphosphides, *Acta Crystallogr.* **33**, 3401 (1977).
- [4] R. Gumeniuk, Structural and physical properties of Remeika phases, in *Handbook on the Physics and Chemistry of Rare Earths* Vol. 54 (Elsevier, Amsterdam, 2018), pp. 43–143.
- [5] M. Baitinger, B. Böhme, A. Ormeci, and Y. Grin, Solid state chemistry of clathrate phases: Crystal structure, chemical bonding and preparation routes, in *The Physics and Chemistry of Inorganic Clathrates*, edited by G. S. Nolas (Springer Netherlands, Dordrecht, 2014), pp. 35–64.
- [6] C. Uher, Skutterudites: Prospective novel thermoelectrics, in *Recent Trends in Thermoelectric Materials Research I*, Semiconductors and Semimetals Vol. 69, edited by T. M. Tritt (Elsevier, Amsterdam, 2001), pp. 139–253.
- [7] A. Maisuradze, M. Nicklas, R. Gumeniuk, C. Baines, W. Schnelle, H. Rosner, A. Leithe-Jasper, Y. Grin, and R. Khasanov, Superfluid density and energy gap function of superconducting $\text{PrPt}_4\text{Ge}_{12}$, *Phys. Rev. Lett.* **103**, 147002 (2009).
- [8] A. Maisuradze, W. Schnelle, R. Khasanov, R. Gumeniuk, M. Nicklas, H. Rosner, A. Leithe-Jasper, Y. Grin, A. Amato, and P. Thalmeier, Evidence for time-reversal symmetry breaking in superconducting $\text{PrPt}_4\text{Ge}_{12}$, *Phys. Rev. B* **82**, 024524 (2010).
- [9] R. Gumeniuk, H. Rosner, W. Schnelle, M. Nicklas, A. Leithe-Jasper, and Y. Grin, Optimization of the superconducting transition temperature of the filled skutterudite $\text{BaPt}_4\text{Ge}_{12}$ by gold substitution, *Phys. Rev. B* **78**, 052504 (2008).
- [10] R. Gumeniuk, W. Schnelle, H. Rosner, M. Nicklas, A. Leithe-Jasper, and Y. Grin, Superconductivity in the platinum germanides $\text{MPt}_4\text{Ge}_{12}$ (M = rare-earth or alkaline-earth metal) with filled skutterudite structure, *Phys. Rev. Lett.* **100**, 017002 (2008).
- [11] R. Gumeniuk, H. Borrmann, A. Ormeci, H. Rosner, W. Schnelle, M. Nicklas, Y. Grin, and A. Leithe-Jasper, Filled platinum germanium skutterudites $\text{MPt}_4\text{Ge}_{12}$ (M = Sr, Ba, La-Nd, Sm, Eu): Crystal structure and chemical bonding, *Z. Kristallogr.* **225**, 531 (2010).
- [12] M. Nicklas, S. Kirchner, R. Borth, R. Gumeniuk, W. Schnelle, H. Rosner, H. Borrmann, A. Leithe-Jasper, Y. Grin, and F. Steglich, Charge-doping-driven evolution of magnetism and non-Fermi-liquid behavior in the filled skutterudite $\text{CePt}_4\text{Ge}_{12-x}\text{Sb}_x$, *Phys. Rev. Lett.* **109**, 236405 (2012).
- [13] H. Sato, Y. Aoki, H. Sugawara, and T. Fukuhara, Peak effect in the superconducting mixed state of $\text{Yb}_3\text{Rh}_4\text{Sn}_{13}$ single crystals, *J. Phys. Soc. Jpn.* **64**, 3175 (1995).
- [14] C. Tomy, G. Balakrishnan, and D. M. Paul, Regions of enhanced pinning in the mixed state of the superconductor $\text{Yb}_3\text{Rh}_4\text{Sn}_{13}$, *Phys. C (Amsterdam, Neth.)* **280**, 1 (1997).
- [15] L. W. Gruenberg and L. Gunther, Fulde-Ferrell effect in type-II superconductors, *Phys. Rev. Lett.* **16**, 996 (1966).
- [16] F. Steglich, R. Modler, P. Gegenwart, M. Deppe, M. Weiden, M. Lang, C. Geibel, T. Lühmann, C. Paulsen, J. Tholence, Y. Ōnuki, M. Tachiki, and S. Takahashi, Experimental evidence for a generalized FFLO state in clean type-II superconductors with short coherence length and enhanced Pauli susceptibility, *Phys. C (Amsterdam, Neth.)* **263**, 498 (1996).
- [17] M. Tachiki, S. Takahashi, P. Gegenwart, M. Weiden, M. Lang, C. Geibel, F. Steglich, R. Modler, C. Paulsen, and Y. Ōnuki, Generalized Fulde-Ferrell-Larkin-Ovchinnikov state in heavy-fermion and intermediate-valence systems, *Z. Phys. B* **100**, 369 (1997).
- [18] A. Haas, D. Wichert, G. Bruls, B. Lüthi, G. Balakrishnan, and D. M. Paul, Elastic properties of superconducting stannides: $\text{Yb}_3\text{Rh}_4\text{Sn}_{13}$ and $\text{Ca}_3\text{Rh}_4\text{Sn}_{13}$, *J. Low Temp. Phys.* **114**, 285 (1999).
- [19] S. Sarkar, S. Banerjee, A. Grover, S. Ramakrishnan, S. Bhattacharya, G. Ravikumar, P. Mishra, V. Sahni, C. Tomy, D. Mck Paul, G. Balakrishnan, and M. Higgins, Elucidation of amorphization of flux line lattice in $\text{Yb}_3\text{Rh}_4\text{Sn}_{13}$, *Phys. C (Amsterdam, Neth.)* **341-348**, 1055 (2000).
- [20] S. Sarkar, S. Ramakrishnan, A. Grover, C. Tomy, G. Balakrishnan, and D. M. Paul, Comparison of thermomagnetic history effects in weakly pinned single crystals of $\text{R}_3\text{Rh}_4\text{Sn}_{13}$ (R = Yb, Ca), *Pramana J. Phys.* **58**, 979 (2002).
- [21] C. Tomy, S. Sarkar, S. Ramakrishnan, A. Grover, G. Balakrishnan, and D. M. Paul, Vortex phase diagrams in $\text{R}_3\text{Rh}_4\text{Sn}_{13}$ (R = Yb, Ca), *Phys. B (Amsterdam, Neth.)* **312-313**, 145 (2002).
- [22] S. Sarkar, C. Tomy, A. D. Thakur, D. M. Paul, S. Ramakrishnan, and A. Grover, Pulverization of the flux line lattice, the phase coexistence and the spinodal temperature of the order-disorder transition in a weakly pinned crystal of $\text{Yb}_3\text{Rh}_4\text{Sn}_{13}$, *Pramana J. Phys.* **66**, 179 (2006).
- [23] S. Kumar, R. P. Singh, A. Thamizhavel, C. V. Tomy, and A. K. Grover, Unveiling of Bragg glass to vortex glass transition by an ac driving force in a single crystal of $\text{Yb}_3\text{Rh}_4\text{Sn}_{13}$, *Supercond. Sci. Technol.* **28**, 085013 (2015).
- [24] S. Kumar, R. P. Singh, A. Thamizhavel, C. V. Tomy, and A. K. Grover, Angular dependent study of spatial order-disorder transitions in the vortex matter of superconducting $\text{Yb}_3\text{Rh}_4\text{Sn}_{13}$, *AIP Conf. Proc.* **1728**, 020625 (2016).
- [25] D. Mazzone, J. L. Gavilano, R. Sibille, M. Ramakrishnan, and M. Kenzelmann, Small-angle neutron scattering study of the mixed state of $\text{Yb}_3\text{Rh}_4\text{Sn}_{13}$, *Phys. Rev. B* **90**, 020507(R) (2014).
- [26] D. G. Mazzone, J. L. Gavilano, R. Sibille, M. Ramakrishnan, C. D. Dewhurst, and M. Kenzelmann, Distinct vortex-glass phases in $\text{Yb}_3\text{Rh}_4\text{Sn}_{13}$ at high and low magnetic fields, *J. Phys.: Condens. Matter* **27**, 245701 (2015).
- [27] M. Schreyer and T. F. Fässler, $\text{Ca}_7\text{Co}_8\text{Sn}_{25}$ - $\text{Ca}_3\text{Co}_4\text{Sn}_{13}$ revised, *Solid State Sci.* **8**, 793 (2006).
- [28] R. Gumeniuk, K. O. Kvashnina, W. Schnelle, A. Leithe-Jasper, and Y. Grin, Magnetic and transport properties of structural variants of Remeika phases: $\text{Th}_3\text{Ir}_4\text{Ge}_{13}$ and $\text{U}_3\text{Ir}_4\text{Ge}_{13}$, *Phys. Rev. B* **91**, 094110 (2015).
- [29] V. Levytskyi, J. Wagler, C. Hennig, M. Feig, T. Weigel, A. Leithe-Jasper, D. Meyer, and R. Gumeniuk, $\text{Sc}_3\text{Ir}_4\text{Si}_{13+x}$ and $\text{Sc}_4\text{Ir}_7\text{Ge}_6$ —the perovskite-related crystal structures, *Z. Kristallogr.* **236**, 313 (2021).

- [30] R. Gumeniuk, L. Akselrud, K. O. Kvashnina, W. Schnelle, A. A. Tsirlin, C. Curfs, H. Rosner, M. Schöneich, U. Burkhardt, U. Schwarz, Y. Grin, and A. Leithe-Jasper, Ca₃Pt_{4+x}Ge_{13-y} and Yb₃Pt₄Ge₁₃: New derivatives of the Pr₃Rh₄Sn₁₃ structure type, *Dalton Trans.* **41**, 6299 (2012).
- [31] R. Gumeniuk, M. Nicklas, L. Akselrud, W. Schnelle, U. Schwarz, A. A. Tsirlin, A. Leithe-Jasper, and Y. Grin, Y₃Pt₄Ge₁₃: A superconductor with a noncentrosymmetric crystal structure, *Phys. Rev. B* **87**, 224502 (2013).
- [32] R. Gumeniuk, M. Schöneich, K. O. Kvashnina, L. Akselrud, A. A. Tsirlin, M. Nicklas, W. Schnelle, O. Janson, Q. Zheng, C. Curfs, U. Burkhardt, U. Schwarz, and A. Leithe-Jasper, Intermetallic germanides with non-centrosymmetric structures derived from the Yb₃Rh₄Sn₁₃ type, *Dalton Trans.* **44**, 5638 (2015).
- [33] V. Levytskyi, E. Svanidze, A. Leithe-Jasper, and R. Gumeniuk, Crystal, electronic structure and physical properties of U₃Rh₄Ge₁₃ and Th₂Rh₃Ge₅, *J. Alloys Compd.* **911**, 165017 (2022).
- [34] M. Feig, L. Akselrud, M. Motylenko, M. Bobnar, J. Wagler, K. O. Kvashnina, V. Levytskyi, D. Rafaja, A. Leithe-Jasper, and R. Gumeniuk, Valence fluctuations in the 3D + 3 modulated Yb₃Co₄Ge₁₃ Remeika phase, *Dalton Trans.* **50**, 13580 (2021).
- [35] M. Feig, W. Carrillo-Cabrera, M. Bobnar, P. Simon, C. Curfs, V. Levytskyi, A. A. Tsirlin, A. Leithe-Jasper, and R. Gumeniuk, Composition dependent polymorphism and superconductivity in Y_{3+x}(Rh,Ir)₄Ge_{13-x}, *Dalton Trans.* **51**, 4734 (2022).
- [36] V. Levytskyi, W. Carrillo-Cabrera, L. Akselrud, B. Kundys, A. Leithe-Jasper, and R. Gumeniuk, Superconductivity of structurally disordered Y₅Ir₆Sn₁₈, *Dalton Trans.* **51**, 10036 (2022).
- [37] A. Bhattacharyya, D. T. Adroja, N. Kase, A. D. Hillier, A. M. Strydom, and J. Akimitsu, Unconventional superconductivity in the cage-type compound Sc₅Rh₆Sn₁₈, *Phys. Rev. B* **98**, 024511 (2018).
- [38] N. Kase, K. Inoue, H. Hayamizu, and J. Akimitsu, Highly anisotropic gap function in a nonmagnetic superconductor Y₅Rh₆Sn₁₈, *J. Phys. Soc. Jpn.* **80**, SA112 (2011).
- [39] N. Kase, S. Kittaka, T. Sakakibara, and J. Akimitsu, Anisotropic superconductivity of the caged compound Y₅Rh₆Sn₁₈ with unusual normal-state electrical resistivity, *JPS Conf. Proc.* **3**, 015042 (2014).
- [40] A. Bhattacharyya, D. Adroja, N. Kase, A. Hillier, J. Akimitsu, and A. Strydom, Unconventional superconductivity in Y₅Rh₆Sn₁₈ probed by muon spin relaxation, *Sci. Rep.* **5**, 12926 (2015).
- [41] Z. Zhang, Y. Xu, C. N. Kuo, X. C. Hong, M. X. Wang, P. L. Cai, J. K. Dong, C. S. Lue, and S. Y. Li, Nodeless superconducting gap in the caged-type superconductors Y₅Rh₆Sn₁₈ and Lu₅Rh₆Sn₁₈, *Supercond. Sci. Technol.* **28**, 105008 (2015).
- [42] M. Feig, W. Schnelle, A. Maisuradze, A. Amon, C. Baines, M. Nicklas, S. Seiro, L. Howald, R. Khasanov, A. Leithe-Jasper, and R. Gumeniuk, Conventional isotropic *s*-wave superconductivity with strong electron-phonon coupling in Sc₅Rh₆Sn₁₈, *Phys. Rev. B* **102**, 024508 (2020).
- [43] D. Kumar, C. N. Kuo, F. Astuti, T. Shang, M. K. Lee, C. S. Lue, I. Watanabe, J. A. T. Barker, T. Shiroka, and L. J. Chang, Nodeless superconductivity in the cage-type superconductor Sc₅Ru₆Sn₁₈ with preserved time-reversal symmetry, *J. Phys.: Condens. Matter* **30**, 315803 (2018).
- [44] V. Levytskyi, M. Feig, L. Akselrud, W. Schnelle, A. Leithe-Jasper, V. Dyadkin, D. Chernyshov, and R. Gumeniuk, Crystal structure and superconducting properties of Sc₅Ir₆Sn₁₈, *J. Phys.: Condens. Matter* **31**, 445603 (2019).
- [45] J. Akimitsu, Towards higher-*T_c* superconductors, *Proc. Jpn. Acad., Ser. B* **95**, 321 (2019).
- [46] S. Miraglia, J. Hodeau, M. Marezio, C. Laviron, M. Ghedira, and G. Espinosa, Nature of the structural distortion and of the chemical bonding in SnM₃Rh₄Sn₁₂ (*M* = La-Gd, Yb, Ca, Sr, and Th), *J. Solid State Chem.* **63**, 358 (1986).
- [47] STOE Powder Software, WinXPow (version 2), Darmstadt, STOE and Cie GmbH, 2001.
- [48] L. Akselrud and Y. Grin, WinCSD: Software package for crystallographic calculations (version 4), *J. Appl. Crystallogr.* **47**, 803 (2014).
- [49] Bruker AXS Inc., DOC-M86-EXX190 D8 QUEST User Manual (2012).
- [50] Bruker AXS Inc., DOC-M86-EXX229 APEX3 Software User Manual (2016).
- [51] K. Koepnik and H. Eschrig, Full-potential nonorthogonal local-orbital minimum-basis band-structure scheme, *Phys. Rev. B* **59**, 1743 (1999).
- [52] J. P. Perdew and Y. Wang, Accurate and simple analytic representation of the electron-gas correlation energy, *Phys. Rev. B* **45**, 13244 (1992).
- [53] V. A. Bruskov, V. K. Pecharskii, and O. I. Bodak, Crystal structure of Y₃Co₄Ge₁₃ compound, *Izv. Akad. Nauk SSSR Neorg. Mater.* **22**, 1471 (1986).
- [54] B. K. Rai, I. W. H. Oswald, J. K. Wang, G. T. McCandless, J. Y. Chan, and E. Morosan, Superconductivity in single crystals of Lu₃T₄Ge_{13-x} (*T* = Co, Rh, Os) and Y₃T₄Ge_{13-x} (*T* = Ir, Rh, Os), *Chem. Mater.* **27**, 2488 (2015).
- [55] B. Sales, B. Chakoumakos, D. Mandrus, and J. Sharp, Atomic displacement parameters and the lattice thermal conductivity of clathrate-like thermoelectric compounds, *J. Solid State Chem.* **146**, 528 (1999).
- [56] J. Emsley, *The Elements* (Clarendon Press, Oxford, 1998).
- [57] R. Pöttgen and D. Johrendt, *Intermetallics: Synthesis, Structure, Function* (Walter de Gruyter GmbH, München, 2014).
- [58] H. Lueken, *Magnetochemie* (Teubner Studienbücher, Stuttgart-Leipzig, 1999).
- [59] R. Gross and A. Marx, *Festkörperphysik* (Oldenbourg Verlag, München, 2012).
- [60] P. Bordet, J. Hodeau, P. Wolfers, G. Krill, F. Weiss, and M. Marezio, Valence fluctuation of Yb in the superconducting ytterbium-rhodium stannides, in *Anomalous Rare Earths and Actinides*, edited by J. Boucherle, J. Flouquet, C. Lacroix, and J. Rossat-Mignod (Elsevier, Amsterdam, 1987), pp. 524–526.
- [61] D.-X. Chen, E. Pardo, and A. Sanchez, Demagnetizing factors of rectangular prisms and ellipsoids, *IEEE Trans. Magn.* **38**, 1742 (2002).
- [62] R. Prozorov and V. G. Kogan, Effective demagnetizing factors of diamagnetic samples of various shapes, *Phys. Rev. Appl.* **10**, 014030 (2018).
- [63] N. Ali, S. B. Woods, G. Kozłowski, and A. Rojek, Resistivity and magnetoresistance of superconducting YbRh_{1.4}Sn_{4.6}, *J. Phys. F: Met. Phys.* **15**, 1547 (1985).

- [64] M. Feig, L. Akselrud, W. Schnelle, V. Dyadkin, D. Chernyshov, A. Ormezi, P. Simon, A. Leithe-Jasper, and R. Gumeniuk, Crystal structure, chemical bonding, and electrical and thermal transport in $\text{Sc}_5\text{Rh}_6\text{Sn}_{18}$, *Dalton Trans.* **49**, 6832 (2020).
- [65] M. Gamža, W. Schnelle, A. Ślebarski, U. Burkhardt, R. Gumeniuk, and H. Rosner, Electronic structure and thermodynamic properties of $\text{Ce}_3\text{Rh}_4\text{Sn}_{13}$ and $\text{La}_3\text{Rh}_4\text{Sn}_{13}$, *J. Phys.: Condens. Matter* **20**, 395208 (2008).
- [66] N. Mott and H. Jones, *The Theory of the Properties of Metals and Alloys* (Dover Publications, New York, 1958).
- [67] E. S. R. Gopal, *Specific Heat at Low Temperatures* (Plenum Press, New York, 1966).
- [68] K. Kadowaki and S. Woods, Universal relationship of the resistivity and specific heat in heavy-fermion compounds, *Solid State Commun.* **58**, 507 (1986).
- [69] N. Tsujii, K. Yoshimura, and K. Kosuge, Deviation from the Kadowaki-Woods relation in Yb-based intermediate-valence systems, *J. Phys.: Condens. Matter* **15**, 1993 (2003).
- [70] U. Köhler, A. P. Pikul, N. Oeschler, T. Westerkamp, A. M. Strydom, and F. Steglich, Low-temperature study of the strongly correlated compound $\text{Ce}_3\text{Rh}_4\text{Sn}_{13}$, *J. Phys.: Condens. Matter* **19**, 386207 (2007).
- [71] Y. Aoki, H. Sato, T. Fukuhara, S. Takayanagi, Y. Ōnuki, and N. Wada, Transport and thermal properties of $\text{U}_3\text{Rh}_4\text{Sn}_{13}$ and $\text{U}_5\text{Rh}_6\text{Sn}_{18}$, *Phys. B (Amsterdam, Neth.)* **186-188**, 738 (1993).
- [72] C. Nagoshi, R. Yamamoto, K. Kuwahara, H. Sagayama, D. Kawana, M. Kohgi, H. Sugawara, Y. Aoki, H. Sato, T. Yokoo, and M. Arai, Magnetic and transport properties of $\text{Gd}_3\text{Ir}_4\text{Sn}_{13}$ with unique crystal structure, *J. Phys. Soc. Jpn.* **75**, 044710 (2006).
- [73] P. Neha, P. Srivastava, Shruti, Sudhesh, and S. Patnaik, Synthesis and characterization of indium doped $\text{La}_3\text{Co}_4\text{Sn}_{13}$ skutterudite superconductor, *AIP Conf. Proc.* **1728**, 020485 (2016).
- [74] O. Prakash, A. Thamizhavel, A. Nigam, and S. Ramakrishnan, Superconductivity in a low carrier density system: A single crystal study of cubic $\text{Y}_3\text{Ru}_4\text{Ge}_{13}$, *Phys. C* **492**, 90 (2013).
- [75] T. Baumgartner, M. Eisterer, H. W. Weber, R. Flükiger, C. Scheuerlein, and L. Bottura, Effects of neutron irradiation on pinning force scaling in state-of-the-art Nb_3Sn wires, *Supercond. Sci. Technol.* **27**, 015005 (2014).
- [76] N. R. Werthamer, E. Helfand, and P. C. Hohenberg, Temperature and purity dependence of the superconducting critical field, H_{c2} . III. Electron spin and spin-orbit effects, *Phys. Rev.* **147**, 295 (1966).
- [77] C. K. Jones, J. K. Hulm, and B. S. Chandrasekhar, Upper critical field of solid solution alloys of the transition elements, *Rev. Mod. Phys.* **36**, 74 (1964).
- [78] E. Talantsev, R. Mataira, and W. Crump, Classifying superconductivity in moiré graphene superlattices, *Sci. Rep.* **10**, 212 (2020).
- [79] T. Klimczuk, F. Ronning, V. Sidorov, R. J. Cava, and J. D. Thompson, Physical properties of the noncentrosymmetric superconductor $\text{Mg}_{10}\text{Ir}_{19}\text{B}_{16}$, *Phys. Rev. Lett.* **99**, 257004 (2007).
- [80] R. Gumeniuk, K. Kvashnina, W. Schnelle, M. Nicklas, H. Borrmann, H. Rosner, Y. Skourski, A. A. Tsirlin, A. Leithe-Jasper, and Y. Grin, Physical properties and valence state of cerium in the filled skutterudite $\text{CePt}_4\text{Ge}_{12}$, *J. Phys.: Condens. Matter* **23**, 465601 (2011).
- [81] E. Zuñiga-Puelles, R. Cardoso-Gil, A. Özden, N. Bulut, V. Svitlyk, C. Himcinschi, J. Kortus, and R. Gumeniuk, Low thermal conductivity in bournonite PbCuSbS_3 : A comprehensive study, *Phys. Rev. B* **106**, 195201 (2022).
- [82] W. Schnelle, A. Leithe-Jasper, H. Rosner, R. Cardoso-Gil, R. Gumeniuk, D. Trots, J. A. Mydosh, and Y. Grin, Magnetic, thermal, and electronic properties of iron-antimony filled skutterudites $M\text{Fe}_4\text{Sb}_{12}$ ($M = \text{Na, K, Ca, Sr, Ba, La, Yb}$), *Phys. Rev. B* **77**, 094421 (2008).
- [83] A. Tari, *The Specific Heat of Matter at Low Temperatures* (Imperial College Press, London, 2003).
- [84] M. Beekman, W. Schnelle, H. Borrmann, M. Baitinger, Y. Grin, and G. S. Nolas, Intrinsic electrical and thermal properties from single crystals of $\text{Na}_{24}\text{Si}_{136}$, *Phys. Rev. Lett.* **104**, 018301 (2010).
- [85] M. M. Koza, A. Leithe-Jasper, H. Rosner, W. Schnelle, H. Mutka, M. R. Johnson, M. Krisch, L. Capogna, and Y. Grin, Vibrational dynamics of the filled skutterudites $M_{1-x}\text{Fe}_4\text{Sb}_{12}$ ($M = \text{Ca, Sr, Ba, and Yb}$): Temperature response, dispersion relation, and material properties, *Phys. Rev. B* **84**, 014306 (2011).
- [86] K. Hattori, Y. Hirayama, and K. Miyake, Local heavy quasiparticle in four-level Kondo model, *J. Phys. Soc. Jpn.* **74**, 3306 (2005).
- [87] Y. Shimono, T. Shibauchi, Y. Kasahara, T. Kato, K. Hashimoto, Y. Matsuda, J. Yamaura, Y. Nagao, and Z. Hiroi, Effects of rattling phonons on the dynamics of quasiparticle excitation in the β -pyrochlore KO_2O_6 superconductor, *Phys. Rev. Lett.* **98**, 257004 (2007).
- [88] Y. Mizukami, M. Kończykowski, O. Tanaka, J. Juraszek, Z. Henkie, T. Cichorek, and T. Shibauchi, Suppression of anharmonic phonons and s-wave superconductivity by defects in the filled skutterudite $\text{LaRu}_4\text{As}_{12}$, *Phys. Rev. Res.* **2**, 043428 (2020).
- [89] M. J. Winarski, B. Wiendlocha, M. Sternik, P. Wiśniewski, J. R. O'Brien, D. Kaczorowski, and T. Klimczuk, Rattling-enhanced superconductivity in $MV_2\text{Al}_{20}$ ($M = \text{Sc, Lu, Y}$) intermetallic cage compounds, *Phys. Rev. B* **93**, 134507 (2016).
- [90] J. Berges, On the scope of McMillan's formula, Master's thesis, Universität Bremen, 2016.
- [91] T. Shang, A. Amon, D. Kasinathan, W. Xie, M. Bobnar, Y. Chen, A. Wang, M. Shi, M. Medarde, H. Q. Yuan, and T. Shiroka, Enhanced T_c and multiband superconductivity in the fully-gapped ReBe_{22} superconductor, *New J. Phys.* **21**, 073034 (2019).
- [92] A. Subedi and D. J. Singh, Electron-phonon superconductivity in noncentrosymmetric LaNiC_2 : First-principles calculations, *Phys. Rev. B* **80**, 092506 (2009).
- [93] V. H. Tran and M. Sahakyan, Specific heat, electrical resistivity and electronic band structure properties of noncentrosymmetric Th_7Fe_3 superconductor, *Sci. Rep.* **7**, 15769 (2017).
- [94] P. B. Allen and R. C. Dynes, Transition temperature of strongly-coupled superconductors reanalyzed, *Phys. Rev. B* **12**, 905 (1975).
- [95] J. P. Carbotte, Properties of boson-exchange superconductors, *Rev. Mod. Phys.* **62**, 1027 (1990).

- [96] S. R. Xie, G. R. Stewart, J. J. Hamlin, P. J. Hirschfeld, and R. G. Hennig, Functional form of the superconducting critical temperature from machine learning, *Phys. Rev. B* **100**, 174513 (2019).
- [97] D. Johnston, Elaboration of the α -model derived from the BCS theory of superconductivity, *Supercond. Sci. Technol.* **26**, 115011 (2013).
- [98] Y. Nakajima, T. Nakagawa, T. Tamegai, and H. Harima, Specific-heat evidence for two-gap superconductivity in the ternary-iron silicide Lu₂Fe₃Si₅, *Phys. Rev. Lett.* **100**, 157001 (2008).
- [99] C. L. Huang, J.-Y. Lin, C. P. Sun, T. K. Lee, J. D. Kim, E. M. Choi, S. I. Lee, and H. D. Yang, Comparative analysis of specific heat of YNi₂B₂C using nodal and two-gap models, *Phys. Rev. B* **73**, 012502 (2006).
- [100] J. Chen, L. Jiao, J. L. Zhang, Y. Chen, L. Yang, M. Nicklas, F. Steglich, and H. Q. Yuan, Evidence for two-gap superconductivity in the non-centrosymmetric compound LaNiC₂, *New J. Phys.* **15**, 053005 (2013).
- [101] J. L. Zhang, G. M. Pang, L. Jiao, M. Nicklas, Y. Chen, Z. F. Weng, M. Smidman, W. Schnelle, A. Leithe-Jasper, A. Maisuradze, C. Baines, R. Khasanov, A. Amato, F. Steglich, R. Gumeniuk, and H. Q. Yuan, Weak interband-coupling superconductivity in the filled skutterudite LaPt₄Ge₁₂, *Phys. Rev. B* **92**, 220503(R) (2015).
- [102] Z. F. Weng, M. Smidman, G. M. Pang, O. Prakash, Y. Chen, Y. J. Zhang, S. Ramakrishnan, and H. Q. Yuan, Nodeless superconductivity and the peak effect in the quasiskutterudites Lu₃Os₄Ge₁₃ and Y₃Ru₄Ge₁₃, *Phys. Rev. B* **95**, 184501 (2017).
- [103] O. Prakash, A. Thamizhavel, and S. Ramakrishnan, Multiband superconductivity in Lu₃Os₄Ge₁₃, *Supercond. Sci. Technol.* **28**, 115012 (2015).
- [104] M. Ichioka, A. Hasegawa, and K. Machida, Vortex lattice effects on low-energy excitations in *d*-wave and *s*-wave superconductors, *Phys. Rev. B* **59**, 184 (1999).
- [105] J. E. Sonier, M. F. Hundley, J. D. Thompson, and J. W. Brill, Low field anomaly in the specific heat of *s*-wave superconductors due to the expansion of the vortex cores, *Phys. Rev. Lett.* **82**, 4914 (1999).
- [106] H. Pfau, M. Nicklas, U. Stockert, R. Gumeniuk, W. Schnelle, A. Leithe-Jasper, Y. Grin, and F. Steglich, Superconducting gap structure of the skutterudite LaPt₄Ge₁₂ probed by specific heat and thermal transport, *Phys. Rev. B* **94**, 054523 (2016).
- [107] B. Bergk, J. Klotz, T. Förster, R. Gumeniuk, A. Leithe-Jasper, V. Lorenz, W. Schnelle, M. Nicklas, H. Rosner, Y. Grin, and J. Wosnitza, Fermi surface studies of the skutterudite superconductors LaPt₄Ge₁₂ and PrPt₄Ge₁₂, *Phys. Rev. B* **99**, 245115 (2019).
- [108] J. Kortus, I. I. Mazin, K. D. Belashchenko, V. P. Antropov, and L. L. Boyer, Superconductivity of metallic boron in MgB₂, *Phys. Rev. Lett.* **86**, 4656 (2001).
- [109] M. Feig, M. Bobnar, I. Veremchuk, C. Hennig, U. Burkhardt, R. Starke, B. Kundys, A. Leithe-Jasper, and R. Gumeniuk, Two-gap superconductivity in Ag_{1-x}Mo₆S₈ Chevrel phase, *J. Phys.: Condens. Matter* **29**, 495603 (2017).
- [110] P. Ravindran, A. Kjekshus, H. Fjellvåg, P. Puschnig, C. Ambrosch-Draxl, L. Nordström, and B. Johansson, Raman and infrared-active phonons in superconducting and non-superconducting rare-earth transition-metal borocarbides from full-potential calculations, *Phys. Rev. B* **67**, 104507 (2003).
- [111] See Supplemental Material at <http://link.aps.org/supplemental/10.1103/PhysRevB.108.214515> for further information.